

## EXPLORING HALO SUBSTRUCTURE WITH GIANT STARS IV: THE EXTENDED STRUCTURE OF THE URSA MINOR DWARF SPHEROIDAL

CHRISTOPHER PALMA<sup>1</sup>, STEVEN R. MAJEWSKI<sup>2</sup>, MICHAEL H. SIEGEL<sup>3,4</sup>, RICHARD J. PATTERSON<sup>4</sup>,  
JAMES C. OSTHEIMER, & ROBERT LINK<sup>5</sup>

Department of Astronomy, University of Virginia

Email: cp4v@virginia.edu, srm4n@virginia.edu, mhs4p@virginia.edu, ricky@virginia.edu, jco9w@virginia.edu,  
rl8z@virginia.edu

*Draft version October 24, 2018*

### ABSTRACT

We present a large area photometric survey of the Ursa Minor dwarf spheroidal galaxy and its environs. This survey is intended to trace the distribution of stars outside the nominal tidal radius of this system. Observations were made with the Washington  $M$ , Washington  $T_2$ , and  $DDO51$  filters, which in combination have been shown previously to provide reliable stellar luminosity classification for K type stars. We identify giant star candidates with the same distance and metallicity as known Ursa Minor RGB stars extending to approximately  $3^\circ$  from the center of the dSph. Comparison to catalogues of stars within the tidal radius of Ursa Minor that have been observed spectroscopically suggests that our photometric luminosity classification is 100% accurate. Over a large fraction of the survey area, our photometry is deep enough that blue horizontal branch stars associated with Ursa Minor can also be identified. The spatial distribution of both the candidate Ursa Minor giant stars and the candidate BHB stars are remarkably similar, and, for both samples, a large fraction of the stars are found outside the nominal tidal radius of Ursa Minor. An isodensity contour map of the surface density of stars within the tidal radius of Ursa Minor reveals several morphological peculiarities: (1) The highest density of dSph stars is not found at the center of symmetry of the outer isodensity contours, but instead is offset southwest of center. (2) The overall shape of the outer contours does not appear to be elliptical, but appears S-shaped. A surface density profile was derived for Ursa Minor and compared to those derived from previous studies. We find that previously determined King profiles with  $\sim 50'$  tidal radii do not fit well the distribution of candidate UMi stars identified in this study, which extends to greater radii than these other surveys. A King profile with a much larger tidal radius produces a reasonable fit, however a power law with index  $-3$  provides an even better fit to the densities at radii greater than  $20'$ . The existence of Ursa Minor associated stars at large distances from the core of the galaxy, the peculiar morphology of the galaxy within its tidal radius, and the shape of its surface density profile all suggest that this system is evolving significantly due to the tidal influence of the Milky Way. However, the photometric data on Ursa Minor stars alone do not allow us to determine if the candidate extratidal stars are now unbound or if they remain bound to the dSph within an extended dark matter halo.

*Subject headings:* galaxies: evolution — galaxies: formation — galaxies: halos — galaxies: individual  
(Ursa Minor dSph) — galaxies: photometry — galaxies: structure

### 1. INTRODUCTION

The study of outer halo objects as tracers of possible substructure of the outer halo is motivated primarily by the Galactic halo formation scenario of Searle & Zinn (1978, hereafter, SZ). In contrast to the Galactic formation model of Eggen, Lynden-Bell, & Sandage (1962), which postulates that the Galaxy formed during a single, rapid collapse of a proto-Galactic cloud, SZ argue that the outer halo of the Galaxy may be made up primarily of stars and stellar systems that formed in transient “fragments” that have subsequently fallen into and been accreted by the Galaxy after the major collapse phase had been completed. While the SZ model for the formation

of the outer halo derives solely from observations of outer halo globular clusters, in the quarter century since the SZ model was introduced, direct observations of outer halo stars have provided support for an accretion origin of at least some of the outer halo. For example, the implied age spread between inner halo and outer halo field blue horizontal branch stars (Preston, Sheckman, & Beers 1991), the measurement of a net retrograde rotation for certain volumes of halo stars (Majewski 1992), and the existence of stellar “moving groups” (e.g., Doinidis & Beers 1989; Majewski et al. 1994, 1996) are all plausible manifestations of the infall and accretion of distinct stellar systems by the Milky Way.

<sup>1</sup> Current Address: Department of Astronomy & Astrophysics, Penn State University, 525 Davey Laboratory, University Park, PA 16802. – cpalma@astro.psu.edu

<sup>2</sup> David and Lucile Packard Foundation Fellow; Cottrell Scholar of the Research Corporation; National Science Foundation CAREER Fellow.

<sup>3</sup> Current Address: Space Telescope Science Institute, 3700 San Martin Drive, Baltimore, MD 21218. – msiegel@stsci.edu

<sup>4</sup> Visiting Astronomer, Kitt Peak National Observatory, National Optical Astronomy Observatories, which is operated by the Association of Universities for Research in Astronomy, Inc. (AURA) under cooperative agreement with the National Science Foundation.

<sup>5</sup> Current Address: Northrop Grumman Information Technology - TASC, 4801 Stonecroft Boulevard, Chantilly, VA 20151

Moreover, the accumulating evidence that the Sagittarius dwarf galaxy (Ibata et al. 1994, 1995) has left stars and globular clusters strewn along its orbit (Mateo et al. 1998; Majewski et al. 1999; Dinescu et al. 2000; Ivezić et al. 2000; Palma, Majewski, & Johnston 2002; Ibata et al. 2001b) provides direct support for the Searle & Zinn (1978) accretion hypothesis. N-body simulations of the evolution of dwarf spheroidal galaxies (dSphs) in the gravitational field of the Milky Way (e.g., McGlynn 1990; Moore & Davis 1994; Oh et al. 1995; Johnston et al. 1996) predict that the tidal disruption of dSphs may occur, and that these galaxies are likely to contribute stars to the outer halo in coherent streams<sup>1</sup>. Recently, significant observational efforts have been devoted to the search for unbound stars associated with other Galactic dSphs (Irwin & Hatzidimitriou 1995; Kuhn et al. 1996; Majewski et al. 2000b; Kocovski & Kuhn 2000; Piatek et al. 2001; Martínez-Delgado et al. 2001; Odenkirchen et al. 2001b) to determine if extratidal stars are a ubiquitous feature in these galaxies, or whether the disruption of Sagittarius is a unique event in the Milky Way’s history.

The study of the internal dynamics and dark matter content of the dSphs is complicated by the unknown extent that the effects of ongoing tidal disruption may have on the equilibrium state of the systems. The central velocity dispersions of the dSph satellites of the Milky Way are all  $\gtrsim 7$  km/sec (Mateo 1998). Assuming that (1) mass follows light, (2) the internal velocity dispersion is isotropic, and (3) the system is in virial equilibrium, these large velocity dispersions imply that the mass-to-light ratio ( $M/L$ ) for the dSphs range up to  $\sim 100$ , an upper limit defined by Draco and Ursa Minor (Hargreaves et al. 1994; Armandroff et al. 1995; Mateo 1998). If these  $M/L$  values are correct, the Galactic satellite dSphs have the highest fractional dark matter content of any known stellar system.

Because such large  $M/L$  values are controversial, it has often been suggested that the velocity dispersions for the dSphs may be inflated by some mechanism. For example, the inclusion of a number of spectroscopic binaries in the sample of stars used to derive the velocity dispersion may inflate the value. However, multiple epoch observations of binaries in Ursa Minor and Draco (Olszewski et al. 1996) and simulations of the effects of binary stars on the velocity dispersions of dSphs (Hargreaves et al. 1996) find that this effect is likely minimal. Kuhn & Miller (1989) proposed another alternative; the varying tidal force felt by a dSph on an elliptical orbit may excite resonances in the galaxy, heating the stars and inflating the velocity dispersion. However, Pryor (1996) disagrees; he claims that this mechanism can not inflate the dispersion by the factor of 10-20 claimed by Kuhn & Miller (1989), and also that the Kuhn & Miller (1989) resonance would create a velocity gradient in the dSph that is not seen in observations of Ursa Minor and Draco.

Although several theoretical studies cast doubt on the assertion that tidal disruption may be responsible for the large  $M/L$  values for the dSphs (Oh et al. 1995; Piatek & Pryor 1995; Johnston et al. 1999), at least one simulation proposes a model where a dSph with no dark matter can

have an observed  $M/L$  of nearly 100 (Klessen & Kroupa 1998). In the high resolution simulations of Klessen & Kroupa (1998), a stellar system is followed for many orbits, until it is nearly completely disrupted, which is in contrast to previous models that were not only of lower resolution but were only followed for short interaction timescales. The remnant of this disruption contains 1% of the initial satellite mass and has properties similar to those observed for the present day dSphs. Furthermore, if the Klessen & Kroupa (1998) remnants are observed with favorable orientations, the central velocity dispersion is large even though the system contains no dark matter. Observations suggest that we are unlikely to be seeing systems like Ursa Minor in the orientation required by this particular family of models, however these models do demonstrate that it is possible for tidally disrupted stellar systems without dark matter to exhibit inflated  $M/L$  values.

Since the identification of tidal tails associated with dSphs bears on both the formation and structure of the Galaxy as well as the structure and evolution of the dark matter halos of dwarf satellite galaxies, we have undertaken a targeted search of the environments around dSph satellites of the Milky Way as one tactic in our exploration of “halo substructure” (Majewski et al. 2000a,b). This paper details the extension of this campaign to the Ursa Minor dwarf spheroidal galaxy.

The study of Ursa Minor is particularly germane to the study of the Galactic tidal effects on dwarf satellite galaxies; Ursa Minor has long been suspected of experiencing ongoing tidal disruption. Hodge & Michie (1969) concluded that Ursa Minor may be “broken up due to the strong galactic tidal force”. Ursa Minor’s morphology, particularly its large ellipticity and clumpy stellar distribution (e.g., Olszewski & Aaronson 1985; Irwin & Hatzidimitriou 1995; Demers et al. 1995; Eskridge & Schweitzer 2001), are indicative of a system far from relaxation. Ursa Minor is also crucial to resolving the controversy over the possible effects tidal disruption may have on internal dSph velocity dispersions since it lies at the extreme end of the range of predicted dark matter content by virtue of its large inferred  $M/L$  ratio and its faint luminosity (Mateo 1998).

In this paper, we present a large area photometric survey of the Ursa Minor (UMi) dSph and its environs (§2) and discuss in detail the selection of candidate Ursa Minor member stars (§3). With our sample of Ursa Minor stars, we analyze the spatial distribution and surface density profile of the galaxy (§4). We conclude that Ursa Minor is surrounded by a significant population of extratidal stars (§5), and discuss the implications of this extended population.

There are several previous large area photometric surveys of Ursa Minor useful as benchmarks for comparison to the survey presented here. The two largest surveys are those of Irwin & Hatzidimitriou (1995, hereafter, IH95) and Kleyna et al. (1998, hereafter, K98). The former survey relied on  $6^\circ \times 6^\circ$  photographic plates of Ursa Minor taken with the Palomar Schmidt telescope. The plates were digitized and an isopleth map of the dSph was created using the stars found within a  $3^\circ \times 3^\circ$  degree region

<sup>1</sup> We note that the Helmi & White (1999) investigation of tidal debris in the *inner* halo finds that stars initially on stream-like orbits will not retain any spatial coherence after a relatively short time, but in order to conserve phase space density, will become increasingly dynamically coherent.

centered on the galaxy. A background stellar density was calculated and subtracted off of the surface density profile for the galaxy, which was calculated from the isopleth map. The latter survey consists of a grid of 27 overlapping  $V$ - and  $I$ -band CCD images of Ursa Minor covering somewhat less than  $1^\circ \times 1^\circ$ . Candidate Ursa Minor stars were separated from the field population using color information. This color selection reduces the background level in the K98 study by approximately a factor of 4 compared to the IH95 survey. The survey presented here complements both of these previous, large surveys in that it covers approximately the same amount of area as IH95, and further reduces the background contamination compared to the deep survey of K98.

## 2. OBSERVATIONS AND PHOTOMETRY

Observations of Ursa Minor were obtained with the Mayall 4 meter telescope at Kitt Peak National Observatory on the nights of 24 to 26 May 1999. The detector in use was the Mosaic camera, a  $4 \times 2$  array of  $2048 \times 4096$  pixel CCDs, which provides a  $36' \times 36'$  field of view. Data on Ursa Minor were taken during photometric conditions. A grid of survey fields was arranged such that adjacent fields overlap by  $5'$ : Three dithered sets of frames were taken in the core of Ursa Minor for additional photometric depth, and a grid of 32 sets of frames were taken surrounding the core (see Figure 1). The objective of the observational program is to detect giant stars in the top few magnitudes of the Ursa Minor giant branch, and thus only short exposures were necessary. For each core field, exposures of 30, 30, and 300 seconds were taken in the Washington  $M$ , Washington  $T_2$ , and  $DDO51$  filters. The grid fields were observed with exposure times of 15, 15, and 150 seconds. All frames were reduced using the MSCRED Mosaic reduction package in IRAF<sup>2</sup>

Instrumental magnitudes for stars detected in all three filters were derived using standard aperture photometry techniques. Ursa Minor is a very low surface density galaxy at high Galactic latitude, so at the relatively shallow depth of our frames, even in the core regions only  $\sim 400 - 800$  objects were detected on each chip of the Mosaic camera. Thus, commonly used techniques of crowded field photometry were not necessary. For each chip of every Mosaic frame, radial profiles were measured for many stars, and the average FWHM for these stars was calculated. Using the IRAF aperture photometry package APHOT, instrumental magnitudes were calculated for every object detected on the chip using an aperture radius 2.5 times the average stellar FWHM for that chip. The average seeing during the observing run was  $\gtrsim 1''$  so the average aperture radius was  $\sim 10 - 11$  pixels. Given an aperture of 11 pixels in radius, 800 stars cover only 0.3% of the area of the chip. In the event that an aperture did include light from a nearby star, this object would likely be rejected from the catalogue using the “structural parameter” described in more detail below.

The instrumental aperture magnitudes for all detected objects were transformed to the standard system defined by Geisler (1990, 1996) standard stars. Instrumental magnitudes for the standard stars were calculated using a pro-

cess identical to the one used for the Ursa Minor survey region stars. Photometric transformation equations of the form:

$$m - M = k_1 + k_2(X) + k_3(M - T_2) \quad (1)$$

were derived that included nightly zero point terms ( $k_1$ ), airmass ( $k_2$ ), and color terms ( $k_3$ ; except in the case of  $T_2$ , which required no color term) from the instrumental magnitudes and colors of the standard stars. For the  $M$  filter, the  $M - T_2$  color was used for deriving the transformation coefficients, and for  $DDO51$ , the  $M - DDO51$  color was used. The equations were derived using software written by C. P. that implements the matrix inversion algorithm of Harris et al. (1981).

After the photometric transformations were applied to the program stars, the calibrated magnitudes of stars measured multiple times (those found in the overlapping areas of each chip) were compared for the purpose of refining the calibration. Although the observations were taken under photometric conditions, the magnitudes of stars measured multiple times have dispersions of  $0.006 - 0.009$  magnitudes, indicating that small errors may remain in the photometry due to small changes in the transparency of the atmosphere or possibly due to the limited accuracy of the airmass coefficient and the airmass measurements. An average offset for each frame was calculated using the measurements of the overlapping stars (for a description of the technique, see Siegel 2001), and these offsets (typically  $< 0.003$  magnitudes) were applied to the calibrated magnitudes, placing the photometry onto a global system with a relative precision of 0.001 magnitudes.

Non-stellar and other problem objects (e.g., close double stars) were removed from the catalogue using a rough structural parameter derived from the aperture photometry. A second magnitude was calculated for every object using an aperture 0.5 times the average FWHM of the stars on the frame. The difference between this magnitude and the 2.5 FWHM aperture magnitude yields an estimate of the concentration of the light from each object, which should be a fixed ratio for stellar images on one frame. Since the scatter around the mean value of this “concentration parameter” increases as the photometric error increases, a running mean and standard deviation of the concentration parameter as a function of magnitude was calculated, and all outliers from the stellar locus were thrown out. Finally, all stars with measurement errors greater than 0.1 in any of the three filters were also removed from the catalogue. Astrometry for all stars was determined by solving for the plate coefficients of each Mosaic chip after matching  $\sim 50$  bright stars per chip with their positions in the USNO-A2.0 catalogue (Monet et al. 1998). Figure 2 displays the spatial distribution (in the USNO-A2.0 astrometric system, J2000.0) of all stars detected in the survey that were retained after the structural parameter and error cuts were applied to the original catalogue.

An  $(M - T_2, M)_0$  color-magnitude diagram (CMD) for all of the stars from Figure 2 is presented in Figure 3. Each star shown in the CMD has been corrected for reddening based on its celestial coordinates and a comparison to the Schlegel et al. (1998) reddening maps. Since the core fields

<sup>2</sup> IRAF is distributed by the National Optical Astronomy Observatories, which are operated by the Association of Universities for Research in Astronomy, Inc., under cooperative agreement with the National Science Foundation.

were observed with exposure times twice as long as the grid fields and also because the observations were taken with varying amounts of moonlight, the limiting magnitude varies across our survey region from  $M_0 < 19.4$  to  $M_0 < 21.0$ . This variation is apparent in the faint end of the CMD, where the core RGB extends to  $M_0 \sim 21$ . The core fields go deep enough that the blue horizontal branch (BHB) stars are well detected at  $M_0 \sim 19.75$ . BHB stars are also detected in the surrounding grid fields, but with larger photometric errors. A plot of the photometric errors as a function of magnitude is presented in Figure 4.

### 3. SELECTION OF CANDIDATE URSA MINOR STARS

We use the technique described in Majewski et al. (2000a) to select giant stars in Ursa Minor and to eliminate the majority of possible sample contaminants. Candidate Ursa Minor giant stars are selected to fulfill two criteria: (1) The stars must have magnesium line/band strengths consistent with those of giant stars, and (2) the stars must have effective temperatures and apparent magnitudes that place them within the giant branch locus of known Ursa Minor giants in the color-magnitude diagram. Only those stars that meet criterion 1 are tested with criterion 2, and only those stars that meet both criteria are selected as candidate Ursa Minor giants.

Table 1 lists the positions and photometry for all candidate UMi RGB stars (§3.2) and UMi BHB stars (§3.6) discussed below.

#### 3.1. Brief Description of the Photometric Selection of Giant Stars

Here is a brief summary of the giant selection technique described in more detail by Majewski et al. (2000a): Each field is observed in three filters, Washington  $M$ , Washington  $T_2$ , and  $DDO51$ . The  $DDO51$  filter is an intermediate band filter centered at 5150 Å that measures the strength of the MgH+Mg $b$  triplet feature in the stellar spectrum. This particular spectral feature is dependent on surface gravity in late type stars, and is thus a good discriminator between K giant stars and K dwarf stars. Geisler (1984) proposed using the Washington  $M$  filter to measure the nearby stellar continuum so that the color  $(M - DDO51)$  can be used for luminosity classification. While the  $(M - DDO51)$  color is primarily sensitive to surface gravity, since more metal-poor giants would be expected to have less Mg absorption than stars of higher metallicity, the index is secondarily sensitive to metal abundance. The equivalent width of the Mg feature depends on stellar effective temperature, as well as gravity and abundance. Since we are specifically interested in K giants (because the sensitivity of the Mg feature to gravity is strongest for this spectral type), we must measure  $T_{eff}$ , also. The  $(M - T_2)$  color is very similar to the standard  $(V - I)$  color (Majewski et al. 2000a), which is a useful measure of stellar effective temperature for late type stars. Therefore, an  $(M - T_2, M - DDO51)$  two-color diagram can be thought of as an  $(T_{eff}, \text{gravity})$  diagram useful for isolating K giant stars from K dwarf stars.

The top panel of Figure 5 is the dereddened two-color diagram (2CD) for all of the stars that were not eliminated by our photometric error or structural parameter cut. Dwarf stars lie along the prominent, elbow-shaped lo-

cus, due to their strong magnesium absorption. The giant region, bounded approximately by the solid line in Figure 5, selects giant stars more metal-poor than  $[\text{Fe}/\text{H}] \sim -0.5$  (Majewski et al. 2000a). For reference, the lower panel of the Figure presents the expected isochrones of giant stars and dwarf stars of various metallicities, which were modified from the synthetic spectra of Paltoglou & Bell (1994) (see Majewski et al. 2000a, for a discussion). The metallicity of Ursa Minor is assumed to be  $[\text{Fe}/\text{H}] \sim -2.2$  based on comparison of its RGB to that of the globular cluster M92 (e.g., Mighell & Burke 1999). However, high resolution spectra of a sample of Ursa Minor giants suggest there is a 0.73 dex spread in the metallicity of Ursa Minor stars with an average of  $[\text{Fe}/\text{H}] = -1.90$  (Shetrone et al. 2001). In any case, at these abundances, the giants in Ursa Minor are expected to be well separated from disk dwarfs in the 2CD.

Stars are considered to be giant candidates if they lie within the bounded giant region in color-color space. The boundary is drawn such that the blue edge is approximately parallel to the dwarf locus, but offset enough so that photometric error will not scatter too many dwarfs into the giant region. Of the 14,100 stars in Figure 3, 1,342 of them are selected as giant candidates using the selection box in Figure 5. The two-color selection process is not perfect at selecting Ursa Minor giants; photometric error can scatter solar metallicity dwarfs into the selection box, and the intrinsic properties of subdwarfs and field giants will place them in the selection box, too. Our calculations (Palma et al. 2002) suggest that the level of contamination of the sample by solar metallicity dwarfs is likely to be  $< 20\%$ .

#### 3.2. Selection of Ursa Minor Giant Candidates

Since the color-color diagram does not easily separate Ursa Minor giants from the several types of potential contaminants mentioned previously, we rely on a second criterion to reduce contamination and to select a more pure sample of Ursa Minor giants. Because the RGB of Ursa Minor appears prominently in the  $(M - T_2, M)_0$  color-magnitude diagram, we can eliminate a large number of contaminant stars selected with the color-color criterion by designating only those giant candidates that also lie along the Ursa Minor RGB in color-magnitude space as Ursa Minor giant candidates. In order to delineate the RGB locus accurately, we have matched stars in our catalogue to those in the proper motion catalogue of Cudworth et al. (2002). Figure 6 shows the  $(M - T_2, M)_0$  color-magnitude diagram for those stars in our catalogue that have proper motion membership probabilities (i.e., their individual proper motions are similar to the mean motion of the galaxy)  $> 75\%$ . The “box” enclosing the proper motion selected Ursa Minor giants defines our second selection criterion; only those color-color selected giants that *also* fall in the color-magnitude RGB box are considered Ursa Minor giant candidates. Applying both photometric selection criteria, color-color and color-magnitude, to our entire sample of 14,100 stars, we have culled 788 candidate Ursa Minor giant stars (see Table 1). A CMD highlighting the selected candidate Ursa Minor giants as well as a plot of their spatial distribution is presented as Figure 7. We note that at this point of the analysis, 202 of the candidate

Ursa Minor giants lie *outside* the IH95 tidal radius of Ursa Minor. We discuss the selection of Ursa Minor BHB star candidates in §3.6.

### 3.3. Effect of Limiting Magnitude Variations

Due to a combination of the presence of several nearby, very bright stars (see Figure 2) and significant moonlight during the observations (the Moon was nearly full), there is a large variation in the limiting magnitude of the various grid fields. Also, three sets of overlapping images of the Ursa Minor core (the RGB box in Figure 6 was defined using stars found only in this region) were taken with exposure times twice as long as those used for the grid fields (this was done so that we could accurately define the locus of the Ursa Minor giant branch in the region with the highest density of member stars). Therefore, the sample of Ursa Minor candidate giant stars presented in Figure 7 is incomplete at the faint end.

In order to accommodate the varying limiting magnitudes and to reflect more realistically the density distribution of Ursa Minor giant candidates, we analyze three separate subsamples of these stars with magnitude limits of  $M_0 = 19.3$ , 19.65, and 20.0. The entire survey area (9.06 square degrees) is included in the  $M_0 \leq 19.3$  sample. In the  $M_0 \leq 19.65$  and  $M_0 \leq 20.0$  subsamples, however, we do not include in our analysis those subfields that have magnitude limits brighter than 19.65 or 20.0, respectively. The  $M_0 \leq 19.65$  subsample covers 8.31 square degrees, while the  $M_0 \leq 20.0$  subsample covers 5.56 square degrees. Figure 8 shows the Ursa Minor giant candidates and areal coverage for each of these three magnitude-limited subsamples.

### 3.4. Evaluation of Giant Background Level

Figure 7 demonstrates that there are field giants (i.e., those stars found to be giants in the color-color diagram that do not lie within the UMi RGB box) in our survey area at a range of  $M_0$  magnitudes. Although we are likely eliminating the majority of dwarf stars from our sample of candidate UMi giants by employing color-color selection, we are unable *a priori* to remove from our sample those field giants and field extreme subdwarfs that happen to have the combination of distance, temperature, and abundance characteristics that place them within the RGB bounding box in Figure 6. Thus, we must evaluate the level of contamination expected from field giants and field subdwarfs.

Majewski et al. (2000b) argue that the number of halo field giants per unit solid angle should be flat to first order if the density of halo stars is roughly an  $R^{-3}$  power law. Therefore, if we were to offset our Ursa Minor RGB bounding box to brighter magnitudes<sup>3</sup>, the number of giants in the box should remain roughly constant as a function of magnitude offset. Indeed, for Carina, this was found to be the case (Majewski et al. 2000b). We repeat this exercise here: We have taken the Ursa Minor RGB box pictured in Figure 6 and offset it to brighter  $M_0$  magnitudes in increments of 0.33 magnitudes. We calculate the number of color-color selected giants that are found in the CMD giant box as a function of magnitude offset of the RGB

box. The calculation was performed separately for each of the three magnitude-limited subsamples, and in each case the RGB box was altered from its shape in Figure 6: the lower limit of the RGB bounding box at magnitude offset 0 was set equal to the magnitude limit of the sample (i.e., 19.3, 19.65, or 20.0).

The results of this analysis are summarized in Table 2. The data in the table illustrate the limitations of this technique for estimating the background; at small magnitude offsets, the RGB bounding box still contains a number of Ursa Minor giant stars. At the largest magnitude offset, the sample is incomplete because of saturation of bright stars on the CCD chips. Unfortunately, this leaves only a few bins for estimating the background. In Table 2 lines have been drawn to indicate the magnitude offset limits of those bins used to derive the background density for each Ursa Minor subsample.

Nevertheless, we take the average of the several bins that do not contain any Ursa Minor giants and that are not affected by saturation at the bright end and determine a background giant density. The error in the background density was calculated assuming a Poissonian probability distribution, that is  $\sigma = \sqrt{N}$ , where  $N$  is the average number of counts for the subsample. A summary of the counts and background levels are presented in Table 3. In each subsample, the number of candidate Ursa Minor giant stars found outside the tidal radius is  $> 3.5$  times the expected number of field giants.

We have further attempted to estimate the expected density of background giants by duplicating our Ursa Minor giant candidate selection on photometry of stars found in an “off” field. Since the “off” field does not contain the Ursa Minor RGB, presumably when we apply our Ursa Minor giant selection criteria to this field, we are *only* detecting field giants. Ostheimer (2002) are conducting a photometric survey of the satellites of the Andromeda Galaxy, and they have provided us with calibrated Washington  $M$ , Washington  $T_2$ , and  $DDO51$  magnitudes for a large sample of stars in the field of And I. The And I giant branch is visible in these data, however, due to the increased distance modulus of this galaxy compared to Ursa Minor (And I lies  $> 800$  kpc from the Milky Way), the tip of the And I RGB is fainter than  $M_0 = 22$ . Thus, when we apply our Ursa Minor RGB selection criteria to these data, we are only selecting Galactic halo giants and subdwarfs. In the  $0.36 \text{ deg}^2$  And I survey region, we find a background density of  $2.8 \pm 2.8 \text{ deg}^{-2}$ ,  $8.3 \pm 4.8 \text{ deg}^{-2}$ , and  $13.9 \pm 6.2 \text{ deg}^{-2}$  using our  $M_0 \leq 19.3$ ,  $M_0 \leq 19.65$ , and  $M_0 \leq 20.0$  RGB selection regions, respectively.

And I and Ursa Minor are at roughly the same galactic longitude,  $l = 122$  and  $l = 105$ , respectively. At these longitudes, giant stars found at  $M \sim 18 - 20$  (corresponding to distances of tens of kpc) would be beyond the disk, so the faint giants in both of these fields are presumably halo stars. Therefore, even though And I is significantly closer to the Galactic plane than is Ursa Minor ( $b = -24.9$  versus  $b = 44.8$ ), as a first approximation, the density of field giants in either of these fields should be similar since the halo is to first order spherical (i.e., the distribution of halo stars is independent of latitude). Although the in-

<sup>3</sup> In principle, this should also work for offsets to fainter magnitudes, but the incompleteness of our survey at the faint end will produce incorrect results for the counts.

ner halo is found to be flattened, the distribution of halo stars outside of roughly  $R_{gc} > 8$  kpc is found to show no significant flattening (e.g., Sommer-Larsen & Zhen 1990; Larsen & Humphreys 1994; Chiba & Beers 2000; Siegel 2001). Since the distant, background giants in the And I field are unlikely to be part of the flattened, inner halo, the background density in the And I field should be comparable to the density of background giants expected in the Ursa Minor field. One caveat that must be considered is that the And I field is much smaller than the Ursa Minor survey region. Thus the background densities derived from this field are based on a small number of stars, and therefore the quantization noise is large (e.g., the background density for the  $M_0 \leq 19.3$  sample is based on 1 star, and therefore the density is  $2.8 \pm 2.8 \text{ deg}^{-2}$ ). Nevertheless, despite their larger uncertainty, the densities derived from the And I data are useful as a “sanity check”. The background densities derived from the And I field for the two fainter subsamples are larger than those estimated using the magnitude offset technique. However, given the limitations of the And I data, these 1 to 1.5  $\sigma$  differences are not unexpected.

Siegel (2001) has derived models for the density laws of Galactic stars in the thin disk, thick disk, and halo stellar populations based on star count observations. According to their best fit Galactic model, the thick disk is not expected to contribute any stars to our UMi RGB selection region, because even at the bright limit of the selection region, a giant star will be  $> 10$  kpc from the Sun. At this distance, the stars will be entirely halo stars. However, contrary to our simplifying assumption, the Galactic latitude of the And I field does increase the density of halo stars in this region. The Siegel (2001) models predict a density of 4 giants per square degree to a depth of  $M_0 \leq 20$  at the Galactic coordinates of Ursa Minor ( $l = 105, b = 45$ ), but the density in the And I region ( $l = 122, b = -25$ ) is predicted to be 12 giants per square degree. These predictions match remarkably well with our measured values, which suggests the methodologies used to derive observational estimates of the background level are reasonable.

For further calculations, we adopt the background densities presented in Table 3. It is reassuring that the background densities estimated from the And I field are  $< 1.5\sigma$  larger than those estimated directly from the Ursa Minor survey region and both are consistent with predictions from the Galactic model of Siegel (2001).

### 3.5. Spectroscopically Verified Ursa Minor Stars

The photometric survey of Ursa Minor that is presented here can be used to provide candidates for spectroscopic followup; radial velocity and metallicity information will allow us to determine if our candidates are *bona fide* members of the Ursa Minor system. Analytical calculations of the expected contamination rate (Palma et al. 2002) as well as our experience with photometric selection of giants in other stellar systems (e.g., Carina, Majewski et al. 2000b; Palma et al. 2002, And I & II, Guhathakurta et al. 2001) support our assumption that the level of contamination in our candidate sample is likely to be low. Here, we present spectroscopic verification that the photometric se-

lection of Ursa Minor stars is efficient at removing dwarfs and field giants from the candidate sample.

Hargreaves et al. (1994) obtained spectra of 60 candidate Ursa Minor stars. Using radial velocities, they confirmed that 45 are Ursa Minor members<sup>6</sup>, 14 are foreground dwarfs, and one is a halo K-giant. Of these 60 stars, 59 are also included in our catalogue. In Figure 9 we present a 2CD and CMD with the spectroscopically verified stars highlighted. All of the stars found in the three deeper pointings of the core region of our survey of Ursa Minor are included in the figure for reference. We note that one of the 45 Ursa Minor members is a known carbon star (CUD122; see the notes to Table 2 in Armandroff et al. 1995), and this star is found near the edge of our giant selection region in color-color space. Another of the member stars passes our color-color giant selection, but lies outside of our Ursa Minor RGB selection region in color-magnitude space.

Armandroff et al. (1995) have also obtained spectra of a sample of candidate Ursa Minor stars. Their catalogue contains a heterogeneously selected set of stars, taken from several sources. There is some overlap between the Hargreaves et al. (1994) and Armandroff et al. (1995) samples. After removing those stars also found in the Hargreaves et al. (1994) catalogue, there are 48 new stars with radial velocities consistent with Ursa Minor membership and 47 stars with disk-like radial velocities (i.e., contaminants) in the Armandroff et al. (1995) catalogue. In Figure 10 we present the 2CD and CMD of the core pointings of Ursa Minor, with the spectroscopically analyzed stars from the Armandroff et al. (1995) catalogue highlighted. Armandroff et al. (1995) include one star, N98 (this star is enclosed in a large circle in Figure 10), in their table of Ursa Minor members even though its velocity ( $-298.7 \text{ km s}^{-1}$ ) is  $\sim 50 \text{ km s}^{-1}$  from the mean velocity of the dSph. They tentatively conclude that this star is a member of UMi, but our photometry suggests that it is not a member. The list of radial velocity members also includes several known carbon stars (enclosed in squares in Figure 10), which fail our photometric giant selection criteria. Finally, several other radial velocity members fail our giant selection even though they are neither marginal candidates, like N98, nor carbon stars. We suspect that several of these may be AGB stars, which our color-magnitude RGB box was designed not to include.

Figures 9 and 10 verify the efficiency of our photometric selection technique. All of the dwarfs in the Hargreaves et al. (1994) catalogue lie outside of our giant selection region. The lone field giant in their sample lies inside our color-color giant selection region, however it lies outside of our adopted Ursa Minor RGB bounding box, and thus we too classify this star as a field giant. Of the 45 *bona fide* Ursa Minor stars found in the Hargreaves et al. (1994) catalogue, we successfully identified 43 of these as Ursa Minor giants, rejecting two (including the carbon star) that lie just outside the edges of our color-color and color-magnitude selection regions. A similar result is seen for the stars in the Armandroff et al. (1995) catalogue. All 47 of their dwarfs lie outside of our giant selection region in color-color space. Of the 48 verified UMi member stars in the Armandroff et al. (1995) catalogue, we successfully

<sup>6</sup> Hargreaves et al. list 46 confirmed Ursa Minor stars in their Table 1, however the star identified as CUD267 is listed twice.

reidentified many of them, however, seven failed either one or both of our selection criteria. The stars that we failed to reidentify as members include a marginal candidate with a velocity significantly different than the mean velocity of UMi and several known carbon stars. We speculate that the UMi member in the Hargreaves et al. (1994) catalogue and several of the UMi members in the Armandroff et al. (1995) catalogue rejected by us may be AGB stars. We note that in a recent study of proper motion-selected stars in Ursa Minor, Eskridge & Schweitzer (2001) found several high probability member stars with colors and magnitudes consistent with those of AGB stars.

Although our photometric selection criteria do not find UMi members with perfect accuracy, the fraction of UMi giants that we miss (“missed detections”) appears to be low and may even be 0% if the majority of these stars are AGB stars and not RGB stars. On the other hand, among this combined sample of 154 stars, we were 100% efficient in rejecting all 61 contaminants (no “false detections”). We conclude from these spectroscopic data that we are (1) efficiently minimizing dwarf contamination, and (2) slightly underestimating (i.e., being somewhat conservative in our selection of) the number of true Ursa Minor giants.

These tests of our photometric selection of giants are encouraging, however we note that the spectroscopically confirmed members of UMi observed to date are found at the bright end of the giant branch. Photometric error is on the average smaller for the bright stars than it is for the faint stars in our sample, so we expect the contamination rate among the bright end to be less than that at the faint end. Several lines of evidence suggest that the overall contamination rate among our giant candidates is low, however, the exact level of contamination of the faint end of the sample remains to be verified.

### 3.6. Blue Horizontal Branch Stars

Astrometry of Ursa Minor stars (Cudworth et al. 1986, and Figure 6) shows that the blue stars found in the CMD of the field containing Ursa Minor have high membership probabilities, thus confirming that these are Ursa Minor blue horizontal branch (BHB) stars. The Ursa Minor BHB stars are prominent in the CMD of this part of the sky because there are very few field stars in the magnitude range of our survey that are as blue,  $(M - T_2)_0 < 0.5$ , as BHB stars. The paucity of field stars in this color range makes the BHB stars an excellent tracer of the spatial distribution of Ursa Minor and a check on the results from the RGB stars.

A BHB star selection region is defined in  $(M - T_2, M)_0$  color-magnitude space such that it encloses the BHB stars with high membership probabilities in the Cudworth et al. (2002) catalogue (see Figure 6). The blue edge of the instability strip appears to occur near  $(M - T_2)_0 \sim 0.4$ , but the BHB selection box extends to  $(M - T_2)_0 = 0.5$ , so we will select some UMi RR Lyrae stars as well as BHB stars. The red edge of the selection box was not designed to cleanly select BHB stars and to exclude red horizontal branch or instability strip stars; instead, the selection box was designed to remain conservatively blueward of the blue edge of the field star population, which is found at  $(M - T_2)_0 \sim 0.7$ . With this conservative red limit, photo-

metric error is unlikely to scatter field stars into the BHB selection box, but we may expect some contamination by UMi variable stars, which is acceptable. It would be useful to be able to analyze the distribution of all of UMi’s stellar populations, including its RR Lyrae stars, red horizontal branch stars, and AGB stars. However, only the RGB stars (which we can cleanly select using two-color and color magnitude criteria) and BHB stars (which we can cleanly select using only a color magnitude box) are easily separated from the Galactic foreground with the data we have available.

When we apply the color-magnitude selection box for BHB stars to our entire survey area, we find 505 candidate BHB stars. In the images of the center of Ursa Minor, the limiting magnitude is  $M_0 < 21$ , and thus all of the BHB stars in the core are well measured, having typical errors significantly less than our  $\sigma < 0.1$  error cut. However, the surrounding grid fields do not go as deep, and in many cases the BHB stars are found at the magnitude limit of a particular frame. In Figure 11 (left panel) we present the CMD of BHB candidate stars found in our survey area that have an error in all three filters less than 0.2 magnitudes (this error cut is still small enough that scatter from the substantial field MSTO should not affect the sample). The right panel of Figure 11 shows the distribution of these candidates on the sky. For reference, the stars in the left panel of Figure 11 are shown with their error bars, most of which fall short of the blue edge of the field star population. We note that a more conservative selection with a  $\sigma \leq 0.1$  error cut reduces the sample to 406 candidate BHB stars and limiting the red edge of the BHB box to  $(M - T_2)_0 = 0.4$  selects 379 candidate BHB stars, 25 of which are outside the 50.6’ tidal radius of UMi. In Table 1 are listed the 406 candidate BHB stars taken from the sample with the more conservative error cut applied.

The correspondence between the spatial distribution of the candidate BHB stars (Figure 11) and that of the candidate RGB stars (Figure 8) is perhaps the best evidence that our sample of candidate giant stars is largely free from contamination. The contamination rate of the candidate BHB star sample is expected to be low, so the similarity between the BHB candidates and the RGB candidates suggests that the contamination rates in these two independently selected samples are comparable. We can estimate the number of potential contaminants in our BHB sample using a similar technique to the one used to estimate the giant background level in §3.4.

We have taken the BHB selection region (which is 0.7 magnitudes thick in  $M_0$ ) and offset it to brighter magnitudes by 0.7, 1.4, and 2.1 magnitudes. The number of stars enclosed in the BHB selection box after these offsets are 59, 23, and 11 stars, respectively. It is likely that the first offset of 0.7 magnitudes is not large enough to avoid UMi variable stars marginally brighter than the BHB population, so 59 stars may be an overestimate for the number of non UMi members we expect in our BHB selection region. The two brighter boxes may not accurately represent the number of faint, blue stars to be found at the magnitude of the UMi horizontal branch. However, if we adopt 59 as an upper limit to the contamination and 11 as a lower limit, the contamination rate of the BHB sample due to field stars should be 2 – 12 %. Although the total contam-

ination rate in the sample of BHB stars appears to be low, we note that the majority of the survey area lies outside the tidal radius of UMi, and thus the fractional contamination rate in the extratidal region is likely to be higher than it is inside the tidal radius of UMi.

#### 4. THE TWO-DIMENSIONAL DISTRIBUTION OF URSA MINOR STARS

Among the population of Galactic satellite dwarf galaxies, Ursa Minor is often considered to be one of the primary candidates for tidal disruption due to its elongated and possibly double-peaked morphology (Olszewski & Aaronson 1985, IH95, Demers et al. 1995), the shape of its surface density profile (IH95), and its spatial and dynamical association with the Magellanic stream of dwarf galaxies (Kunkel & Demers 1976; Lynden-Bell 1982b; Lynden-Bell & Lynden-Bell 1995; Majewski, Phelps, & Rich 1996; Palma, Majewski, & Johnston 2002). The spatial distributions of different samples of candidate Ursa Minor stars presented here (Figures 7, 8, and 11); all show a significant extended population, which lends support to the tidal disruption hypothesis. Alternatively, these UMi stars may be bound within the potential of an extended dark matter halo (cf. Burkert 1997). In the following sections, we analyze the morphology and surface density profile for Ursa Minor derived from the samples of candidate stars discussed earlier to test the predictions of the Galactic tidal interaction scenario.

##### 4.1. Morphological Peculiarities

The majority of the satellite galaxies of the Milky Way are dwarf spheroidals; this nomenclature derives from their shapes, which are for the most part spherical or ellipsoidal (e.g., IH95). Since the dSphs are not isolated systems, but are instead evolving in the gravitational potential of the Milky Way (which varies as seen by a dSph in a non-circular orbit), it is feasible that upon closer examination, their current morphologies may reflect the effects of this evolution. The two dSphs at the extremes of morphology are Leo II, at  $R_{gc} \sim 200$  kpc, which is mostly spherical (Siegel et al. 2000), and Sagittarius, at  $R_{gc} \sim 16$  kpc, which has tidal streams of stars and clusters that encircle the Galaxy (Mateo et al. 1998; Majewski et al. 1999; Ivezić et al. 2000; Dinescu et al. 2000; Ibata et al. 2001b). Since Ursa Minor is the closest dSph to the Galactic Center ( $R_{gc} \sim 65$  kpc) after Sagittarius, its morphology might be expected to be more similar to Sgr than Leo II.

The peculiar morphology of Ursa Minor is well documented; Olszewski & Aaronson (1985) were the first to propose that the core of the galaxy contains substructure in the form of two clumps of stars. Subsequently, Demers et al. (1995) identified an off-center clump of 78 stars in their study of a small region in the core. IH95 confirmed the presence of two clumps of stars in the core of Ursa Minor, separated by an angular distance of  $\sim 15'$ . From observations of the largest area prior to our survey, K98 detected substructure in the shape of their isodensity contours of Ursa Minor. However, the authors concluded that the secondary peak visible in their contour plot (and also detected in previous surveys; Olszewski & Aaronson 1985, IH95) is not detected at a statistically significant level. On the other hand, relying on a proper motion selected

sample of UMi stars that is expected to be nearly free of contamination, Eskridge & Schweitzer (2001) instead find that the internal substructure in UMi is statistically significant. The most recent observations of the core by Battinelli & Demers (1999) were made with the WFPC2 camera on the *Hubble Space Telescope*. With the high resolution afforded by the *HST* and the depth of the data ( $m_{F606W} \leq 24$ ), Battinelli & Demers (1999) resolved the density peak near the center, and claim that the enhancement is due to a ring of stars surrounding a low density void.

Figure 12 shows an isodensity contour plot for the central region of Ursa Minor from our data. The sample of candidate Ursa Minor stars used to create this image is a combination of the  $M_0 \leq 20.0$  RGB candidates from Figure 8 (lower left panel) and the BHB candidates with magnitude errors in each filter  $\leq 0.1$  mag (since the contour image includes almost entirely stars found in the longer exposure time core fields, all of the BHB stars have errors below this limit). RGB and BHB candidates found in the excluded fields in the lower left panel of Figure 8 are not included due to the incompleteness problems in these fields at the magnitude of the HB. Since the density of Ursa Minor stars in these outer grid fields is low, this areal restriction does not change the appearance of the isodensity contours (the hatched region that indicates area excluded from the survey region for  $M_0 \leq 20.0$  in Figure 8 is reproduced in Figure 12; none of the contours lie within the excluded region). The final sample used contains 1001 stars. The image was created using the following steps: (1) The equatorial coordinates of each star were converted to Cartesian coordinates using a tangential projection centered at the K98 center of Ursa Minor ( $\alpha_{2000.0}, \delta_{2000.0} = 15^{\text{h}}09^{\text{m}}03.9^{\text{s}}, 67^{\circ}13'51''$ ). (2) The tangential plane was partitioned into a grid of  $50 \times 50$  “pixels” each  $4.2'$  on a side. (3) The number of stars in each pixel were counted, creating a two-dimensional array suitable for presentation as a contour plot.

Direct comparison between the contour plot presented here and previous work is complicated by the difference in sample selection. Previous studies of Ursa Minor included many more stars than are presented here, because these studies all probed deeper into the luminosity function of Ursa Minor, reaching further down the giant branch (IH95, K98), sometimes to the main sequence turn off (Olszewski & Aaronson 1985; Battinelli & Demers 1999). However, in each of these studies, only single filter or dual filter data was taken, and we would argue that the level of contamination by non-Ursa Minor stars in these previous presentations of the isodensity contours of Ursa Minor are less certain than our own work, which is guided by the ability to discriminate between Galactic stars and Ursa Minor stars with the use of Washington+DDO51 photometry. Thus, we expect the signal to noise in the outer isodensity contours presented here to be better than previously available representations of Ursa Minor, while the signal to noise in the core region is likely to be similar.

The isodensity map of Ursa Minor shows several interesting features. We do detect two off-center peaks in the spatial distribution: the strongest just west of the center, and a secondary peak to the northeast. Within the IH95 core radius of  $15.8'$ , the mean number of UMi candidate



stars per pixel is 13.5. Due to the small number of pixels within this area and the presence of the peaks within the core region, the standard deviation in the number of UMi stars per pixel within the core radius is  $\sigma = 9.8$ . Therefore, the primary peak (34 counts) is a  $2\sigma$  peak above the mean for the core region, but the secondary peak (27 counts) is only a  $1.5\sigma$  peak. However, the stars that make up the primary peak are spread out over two pixels of 34 and 33 stars each, so with slightly coarser binning or with a slight change in center, this peak is found at much higher significance. The secondary peak is more diffuse, and remains at  $\sim 1.5\sigma$  even if the bin size or phasing changes. Thus, as was found by K98 with their data, the secondary peak is not detected with high statistical significance in our data, but both surveys agree about the existence of this density enhancement at a similar level. Since several surveys have now identified this second peak in UMi, albeit at low statistical significance in most cases, it seems likely that the secondary density peak is a real feature in the dSph, and the significance of it in any particular survey is limited by the number of stars in Ursa Minor available at the magnitude limits probed by most observers. Another feature that is prominent in our isodensity map that is seen to a lesser degree in IH95 is the “hook” in the northeast portion of Ursa Minor. The stars that form the secondary peak are elongated not along the major axis, but along a line at a position angle between that of the major and minor axes. The bend in the contours is in the direction of the orbital motion of Ursa Minor, which may indicate this clump of stars is being stretched by the Galactic tidal field.

In an attempt to reduce the noise of the isodensity contours introduced by the gridding process, we have smoothed the stellar positions using a Gaussian kernel, creating the contour plot seen in Figure 13. The following process was used for the smoothing: (1) Each star was replaced by a two-dimensional square array  $3.4'$  on a side. (2) The square array was filled with the values calculated for a two-dimensional Gaussian with center at the position of the star and a large FWHM, such that the values in the square array were almost flat. (3) The survey area was then partitioned into a finer grid of  $100 \times 100$  “pixels” each  $2.1'$  on a side, and the number of counts from each Gaussian smoothed “star” in each pixel was calculated.

The smoothed representation of the stellar spatial distribution reduces the significance of the secondary peak further, while enhancing the primary peak, and reinforcing that the primary peak is truly the location of the highest surface density of UMi stars. The primary peak is offset from the center of UMi as defined by the outer contours, and it is also offset from the center of symmetry of the “ring” of UMi stars (plotted as a filled square) seen in the HST images of Ursa Minor by Battinelli & Demers (1999). The peak isodensity contours are less elliptical than the outer contours, and their position angle is different as well. Overall, the contours appear to twist at increased distance from the peak contours, giving the galaxy an overall “S-shaped” morphology.

In order to test the significance of the S-shaped morphology of the UMi isodensity map, we have compared the distribution of UMi stars within the elliptical boundary defined to have tidal radius along the semi-major axis of  $50.6'$

to a model for a dSph with surface density distributed according to the ellipticized single-component King model as parameterized by K98. Our model was created by selecting points randomly within the elliptical boundary of UMi (drawn in Figure 12). Using a rejection algorithm (see §7.3 in Press et al. 1992), the random points were selected such that their surface density distribution follows that for the ellipticized King profile of UMi. Among the 1001 stars used to create Figure 12, 847 of them are within the elliptical boundary of UMi. In order to increase the signal to noise of the model, it was generated with 10 times this number of stars, or 8470 points. In order to test the null hypothesis that the UMi stars are drawn from an ellipticized King model parent distribution, we compared the distribution of the 847 UMi stars to the 8470 model stars with the two-dimensional Kolmogorov-Smirnov test (Fasano & Franceschini 1987; Press et al. 1992). The probability that the 847 UMi stars are drawn from the same parent distribution as the model is  $\ll 1\%$ . Thus, we conclude that the distribution of stars used to create Figure 12 deviates from a symmetric, ellipsoidal model at a statistically significant level.

#### 4.2. Surface Density Profile

For the purpose of measuring the important physical quantities such as the mass or luminosity of a dSph, model fits are usually made to the surface density profile of dSph stars. It is generally assumed that dSph galaxies can be fit with a King profile, however other models, such as exponentials or Sérsic profiles, are used as well. While it can be argued which type of model is the most reasonable to use in fitting a dSph profile, most previous studies of UMi have fit King profiles to the observed stellar distribution (e.g., IH95, K98). In this section, we use the structural parameters for UMi derived from King profile fits by IH95 and K98 to calculate a new surface density profile of UMi. We note here that there is an apparent discrepancy between the IH95 and K98 fits to UMi that is relevant to the search for extratidal stars associated with this dSph; the tidal radii derived from these two studies differ significantly. IH95 derived a tidal radius of  $r_t = 50.6'$ , while K98 quote a value of  $r_t = 34.0'$ . However, the former is a semi-major axis value, while the latter is a true “radius”, that is, it is the tidal radius expected if Ursa Minor were circular and not elliptical. Converting the K98 value to a semi-major axis value ( $a_t = r_t \times \sqrt{1-\epsilon}$ ) gives  $50.9'$ , almost identical to the IH95 measurement. For the purpose of illustration of the structure of UMi, the position angle and ellipticity parameters from the K98 study are adopted, however, we adopt the semi-major axis value of  $r_t = 50.6'$ . We adopted these structural parameters because the K98 study is the largest area survey prior to our own that probes the largest dynamic range of UMi stellar density. The ellipse seen in Figures 2, 7, 8, and 11 was constructed using these shape parameters.

Using the standard method for estimating stellar densities in dSphs (cf. IH95), we have constructed surface density profiles of the Ursa Minor dSph using the three magnitude-limited subsamples of UMi RGB candidates seen in Figure 8. Due to the more serious completeness problems in the sample of BHB candidates (several of the survey fields don’t go deep enough or blue enough to detect

UMi BHB stars at all) no profile was created using these stars. However, by visual inspection alone the distribution of BHB stars (Figure 11) appears quite similar to that of the RGB stars (Figure 8). For the RGB stars, the densities were calculated by first counting our candidate Ursa Minor giant stars in elliptical annuli of successively larger semi-major axis. The shape of the annuli correspond to the structural parameters mentioned previously (derived from the shallow data for Ursa Minor by K98; specifically, an ellipticity of 0.554, a position angle of  $49.4^\circ$ , and a center of B1950.0  $15^h08^m27.5^s$ ,  $+67^\circ25'12''$  were adopted). The center of Ursa Minor is not well-defined, however, the galaxy is diffuse at low densities, and small changes in the location of the center do not affect significantly the number of stars in a given annulus. The star counts in each annulus were converted to densities ( $\text{arcmin}^{-2}$ ) by dividing by the area of the annulus. The background was removed by subtracting off the mean background density for each subsample (Table 3) from the Ursa Minor density calculated for each annulus. Within the core radius of IH95, we space our annuli in intervals of  $3.4'$ , but in order to improve our signal to noise, outside a radius of  $13.6'$ , the annuli are spaced at  $6.8'$ . The inner and outer semi-major axes of the annuli, the area of each annulus, and the raw Ursa Minor RGB counts are given in Table 4. For the  $M_0 \leq 19.3$  UMi RGB candidates, the outermost annulus that fits completely within the boundaries of the survey region has  $a = 95.2'$ . The survey fields not included in the fainter samples due to photometric incompleteness restrict the size of the largest annulus that fits completely within the boundary region to  $61.2'$  and  $54.4'$  for the  $M_0 \leq 19.65$  and  $M_0 \leq 20.0$  samples, respectively. We made star counts in annuli with outer radii up to  $204.0'$ , and we determined numerically the fractional area of each annulus enclosed within our survey region. Thus, Table 4 includes star counts for each subsample out to  $r = 204.0'$ , however, the increasingly reduced fractional area in the outermost annuli introduces increasingly more noise into those bins. For this reason, the outermost annuli ( $r_{\text{outer}} > 95.2'$ ) have been spaced at  $27.2'$ .

Figure 14 presents the radial surface density profile derived for Ursa Minor from the star counts in Table 4. Shown in the upper panel are the results for the three magnitude-limited subsamples of Ursa Minor giant candidates: the  $M_0 \leq 19.3$  sample (filled circles), the  $M_0 \leq 19.65$  sample (filled triangles), and the  $M_0 \leq 20.0$  sample (filled diamonds). In both panels, each set of points was offset vertically by one order of magnitude (i.e., one tick mark along the logarithmic y-axis) in order to reduce confusion due to overlapping points. In the upper panel, those points that are derived from annuli that do not fit completely within the boundaries of our survey region (and thus may be susceptible to local density fluctuations since they are not completely sampled) are represented as open symbols. In addition, the deeper, background corrected Ursa Minor star counts of IH95 are shown (filled stars), for comparison. After normalizing these four profiles so that their densities at  $R \sim 6.8'$  are all equal to 1.0 (this point was chosen since it is at high signal to noise and the scatter at this radius between our three subsamples is low), they can be more easily compared (Figure 14, lower panel). The IH95 King profile fit has tidal radius  $r_t = 50.6'$ ; this

fit is plotted as a solid line in the lower panel of Figure 14. Although this fit follows the IH95 points well, our star counts appear to deviate away from the fit; the densities for each magnitude limited sample measured in this study are found to be systematically larger than the fit for all radii  $r > 20.4'$ . The King profile derived by IH95 is an especially poor fit to the bright sample of Ursa Minor giant candidates; past  $20.4'$ , these points are fit very well by a power law  $r^{-\gamma}$  with index  $\gamma = 3.0$  (the dashed line in the lower panel of Figure 14).

But IH95 also noted that a King profile was not necessarily a good fit to their data. The shape of the IH95 surface density profile is similar to the model King profile out to distances of  $\sim 30'$ , beyond which their signal to noise becomes small. In order to overcome the signal to noise limitations, they averaged the counts in several radial bins past the  $30'$  limit (we reproduced these points using the data in their Table 3 and plot them in our Figure 14). The average density in the  $\sim 36'$ ,  $\sim 46'$ , and  $\sim 56'$  bins of IH95 is significantly higher than predicted by the King model. The stars that contribute to the deviation from the King profile fit are referred to as “extra-tidal stars” by IH95, and they suggest these stars may be indicative of ongoing tidal disruption of Ursa Minor by the Galaxy.

Numerical simulations of tidally disturbed stellar systems in the outer halo of the Galaxy (Johnston et al. 1999) predict that the surface density profile should exhibit a “break” in the density fall-off, beyond which the unbound stars begin to contribute more signal to the profile than do the bound stars, eventually becoming the dominant population. Beyond this break, the model predicts that the stellar density should follow a shallow power law dropoff of  $\Sigma(r) \sim r^{-1}$ . The IH95 star count profile of Ursa Minor is quite similar to those derived from the numerical simulations of Johnston et al. (1999). However, the profiles constructed using the Ursa Minor giant candidates identified in this study do *not* show a sharp break in the profile followed by a shallow dropoff in the stellar densities. Instead, the profile deviates slowly from the King profile (suggesting that an increased tidal and/or core radius King profile compared to that of IH95 would provide a better fit), and then it follows a  $\Sigma(r) \sim r^{-3}$  power law decay in the outer regions that is steeper than the predictions for the density fall-off of extratidal stars made by Johnston et al. (1999). The bright subsample shows the smoothest profile, however, the two fainter subsamples perhaps show a break at roughly  $40'$ . The deviation in density near this potential break point is not large compared to the error bars, though, so we hesitate to conclude with any certainty that this is indeed a break as predicted in the simulations of disrupting satellites. The stellar densities in the two fainter subsamples for radii past this potential break still follow a  $\sim r^{-3}$  power law, however.

Due to the east/west asymmetry and other morphological peculiarities seen in Ursa Minor, it is possible that the usual methodology employed to study the global profiles of dwarf galaxies is less appropriate in the case of UMi. The surface density profile derived from the global spatial distribution of giants will not represent local features well. To investigate possible variations induced by nonsymmetry, we have derived radial surface density profiles for all UMi giant stars east of the minor axis and also for all

UMi giant stars west of the minor axis (the adopted center of UMi is found between the two density peaks, thus the primary density peak is found west of the minor axis and the secondary peak is east of the minor axis). The method employed was identical to that used to create Figure 14, however, in this case candidate UMi giant stars were counted in semi-ellipses on either side of the minor axis. Also, due to differing sample completeness on either side of Ursa Minor, only those annuli that completely fit within the survey boundaries are used in this analysis.

The morphological variations, evident in the surface density maps (Figures 12 and 13), are clearly manifest in the comparison of the radial profiles constructed from stars east and west of the minor axis. There are two major differences between the eastern and western radial profiles apparent in all three panels of Figure 15.

- The innermost point of the western profile is consistently higher than the corresponding point on the eastern profile. This reflects the presence of the strong peak in the star counts in the western half of UMi. Within the core region (semi-major axis  $\leq 13.6'$ ), the density falls off more quickly on the western half than it does on the eastern half. This is another way of saying the core region is more centrally concentrated toward the western side.
- Outside of the core region (semi-major axis  $\geq 20.4'$ ), the three western profiles follow the roughly  $r^{-3}$  power law decay seen in the global profile (Figure 14). However, in all three eastern profiles, the  $34'$  point is enhanced compared to the corresponding point on the western profile, while the  $40.8'$  point is suppressed. The change in these two points makes the eastern profiles appear to break, as seen in numerical simulations of tidally disrupting systems (Johnston et al. 1999) and in observations of Carina (Majewski et al. 2000b). A more recent surface density profile for Ursa Minor has been produced by Martínez-Delgado et al. (2001), and they also find a similar jump between their  $30'$  and  $40'$  points, suggesting that the feature seen in Figure 15 is real (and also that our sample of UMi stars, selected completely independently, traces the same structures as does their sample). For the two brighter samples (top two panels of Figure 15), the power law index of the points past the break on the eastern profiles is shallower ( $\sim r^{-2}$ ) than for these same points on the western profiles ( $\sim r^{-3}$ ).

Unfortunately, these differences between the eastern and western radial profiles are at low statistical significance. However, the eastern profile suggests the possibility that, at least locally, the radial profile of Ursa Minor breaks at  $r = 34'$ . That this break radius also corresponds to the break radius observed by IH95 suggests the adoption of about  $34'$  as the beginning of significant contribution by unbound stars. We may use this radius to estimate the mass loss rate of Ursa Minor by the formalism of Johnston et al. (1999). The estimated mass loss rate quoted for Ursa Minor in Johnston et al. (1999) of 32% uses the

value of  $r_{break}$  from IH95. If we adopt  $r_{break} = 34.0'$  and  $r_{xt} = 95.2'$  (the outermost annulus measured with high statistical significance in the bright subsample), then from the data in Table 4 and in Table 4 of Johnston et al. (1999) we find a fractional mass-loss rate of  $df/dt_1 = 0.33 \text{ Gyr}^{-1}$ . If this stellar mass loss rate has been roughly constant over the lifetime of the galaxy, then the mass of Ursa Minor was  $0.67^{-N}$  times larger  $N$  Gyr in the past. If the central velocity dispersion for Ursa Minor and its inferred  $M/L$  ratio of 79 are correct, then the mass of this dSph is currently  $\sim 2 \times 10^7 M_\odot$  (Mateo 1998), and if total mass loss tracks stellar mass loss, a constant  $df/dt$  suggests that UMi may have been  $> 10^9$  solar masses 10 Gyr ago. However, the exact mass of Ursa Minor, the amount of mass loss by the dSph to the halo, and the form (i.e., stars and/or dark matter) of the mass lost depend strongly on input assumptions, and thus the exact mass of stars and dark matter deposited in the Galactic halo by Ursa Minor is highly uncertain.

Stars that are being removed from Ursa Minor will wind up in the Galactic halo, and they may be detectable as an accreted population; for example, by their kinematics (cf. the moving group of Majewski et al. 1996). The Galactic halo is made up predominantly of old, metal-poor stars with little or no net rotation around the Galaxy. However, there is evidence that the distant outer halo stars may have a net retrograde rotation (Majewski 1992), which can not occur in a population formed during a monolithic collapse. This retrograde rotation has been confirmed (Majewski 1992; Carney et al. 1996), and, furthermore, metallicity information suggests an additional difference between the retrograde component of the halo: The metallicity of the “high halo” retrograde stars peaks around  $[\text{Fe}/\text{H}] \sim -2.0$ , while the mean metallicity for the “low halo” is  $[\text{Fe}/\text{H}] \sim -1.6$ . Both Majewski (1992) and Carney et al. (1996) suggest that the retrograde rotation may be attributable to accretion by the Galaxy of other stellar systems, and the metallicity differences between the retrograde stars and the majority of the halo perhaps provide support for this hypothesis. It has been argued (Unavane, Wyse, & Gilmore 1996) that the halo can only contain a small percentage of stars accreted from the dSphs, particularly if the typical accreted dSph had a stellar population similar to the present day populations of Carina and Fornax, which have dominant *intermediate* age populations. However, Ursa Minor apparently contains only a single old stellar population (e.g., Mateo 1998; Feltzing et al. 1999) with a mean metallicity near  $[\text{Fe}/\text{H}] \sim -2.0$  (Shetrone et al. 2001). Thus, those Ursa Minor stars accreted into the halo will be virtually indistinguishable from the Galactic “high halo” population.

Since Ursa Minor has a prominent population of BHB stars (unlike many of the other dSphs), the disruption of UMi will contribute BHB stars to the Galactic halo. A large scale photographic study of the Galaxy (Beers et al. 1985) has been used to identify candidate blue “field horizontal branch” (FHB) stars (e.g., Preston, Sackett, & Beers 1991; Wilhelm et al. 1999). The density of these stars on the sky is low, however, and the magnitude limit of the photographic plates ( $B \sim 16$ ) is such that these FHB stars are mostly nearby and the outer halo is not sampled. A catalogue of more distant FHB stars has been

created (Flynn et al. 1995), however, it covers far less area than the earlier study of Beers et al. (1985), and it only includes a few stars more distant than 20 kpc. Thus, the overall distribution of FHB stars in the *outer* halo remains unknown. While the density of FHB stars in outer halo streams possibly can be used to constrain the disruption history of UMi, the lack of a well-defined, complete sample of distant FHB stars prevents a comparison at this time.

We note that the Sloan Digital Sky Survey (SDSS; York et al. 2000) is expected to provide a catalogue of outer halo FHB stars useful for mapping the structure of the Galactic halo. Some SDSS data (nearly 400 deg<sup>2</sup>) on A-colored stars (Yanny et al. 2000), both FHB stars and blue stragglers, have been used to map out substructure in the halo. Yanny et al. (2000) determine the masses of two large substructures that they have identified to be a few  $\times 10^6 M_\odot$ , and suggest that they may be streamers produced by tidal disruption of dwarf galaxies. Using additional SDSS data on F-type stars, Newberg et al. (2002) confirm the existence of the Yanny et al. (2000) substructures, and associate them with streams from the Sagittarius dwarf galaxy. A similar search for FHB star streams potentially associated with UMi is feasible when more SDSS data become available.

#### 4.3. Implications for the Dark Matter Content of UMi

The morphology and radial profile of Ursa Minor appear to support the hypothesis that this stellar system is being influenced strongly by the tidal field of the Milky Way. This accumulated evidence leads us to question the widely accepted notion that the dSph is dark matter dominated. Burkert (1997) has proposed that UMi can only be dark matter dominated if the “extratidal” stars are not in fact extratidal; that is, if the dark matter halo is very massive and much more spatially extended than the stellar component of the dSph, and the stars identified in this study and others as “extratidal” are bound within the potential of the dark matter halo. However, if the Burkert (1997) model for the dSph is the correct one, it suggests that the Milky Way tidal field should only be altering the morphology of the dark matter component of UMi, since the stars must be comfortably within the tidal radius of the dark matter halo. In this scenario, one expects that the stars will be distributed smoothly within the dSph gravitational potential, the shape of which is determined by the dominant dark matter component. However, it is clear that the stellar component of UMi is far from smooth, and this is a problem for the models where the dSph is embedded in a massive, extended dark matter halo model.

While the morphological evidence for ongoing tidal disruption of Ursa Minor appears strong, there does not yet appear to be a satisfactory explanation for producing an inflated velocity dispersion in a disrupting system. Although the dSph model of Klessen & Kroupa (1998) can produce inflated velocity dispersions for unbound systems that extend along the line of sight, this is not applicable to our sight line with Ursa Minor, and it also predicts that the width of the horizontal branch should be inflated due to the distance modulus variations of the unbound stars found along the line of sight. We can rule out any width of the HB larger than  $\sim 0.3$  magnitudes (although the photometric errors at the level of the HB are relatively

large), which is smaller than the  $\sim 1$  magnitude width seen in simulated data by Klessen & Kroupa (1998). Also, while we have attributed the asymmetric morphology of the Ursa Minor RGB and BHB stars to the tidal influence of the Milky Way, it may be possible to construct a non-standard dark matter halo model in which the morphology of the stellar population of Ursa Minor could arise. The current state of our knowledge of the extended distribution of the stars associated with Ursa Minor alone does not appear to allow us to rule out the presence of a large dark matter component for this dSph.

Relying on the current data on UMi, we can however address the accuracy of the reported values of  $M/L$  for the dSph. The standard method for measuring  $M/L$  requires an estimate of the total mass derived from the core velocity dispersion, and an estimate of the total luminosity estimated from observations. Since the dSphs for the most part cover large areas of the sky, it is difficult to determine their luminosities accurately. For example, IH95 estimated the total luminosity of Ursa Minor by using the King profile fit to define an aperture expected to enclose 90% of the light. In their §7.1.1, they point out that for UMi, the largest fraction of the error budget in their  $M/L$  estimate of  $95 \pm 43$  is due to the error in  $L_{tot}$ , which they calculate to be  $2.0 \pm 0.9 \times 10^5 L_\odot$ . Clearly, this estimate hinges on the accuracy of the King profile in defining the extent of Ursa Minor. However, this profile was fit to data that were background limited after  $\sim 30'$ . Since the current sample of UMi stars has eliminated much of the background, we are able to trace the dSph to radii of  $\gtrsim 100'$  with reasonable signal-to-noise.

Assuming that a King profile is a reasonable model for fitting the profile of UMi (our data suggest this may not be true), we have used a Maximum Likelihood technique (similar to the one presented in K98) to fit the data points presented in Figure 14. The best fit King model to our  $M_0 \leq 20.0$  sample of UMi RGB candidates has  $r_t = 77.9' \pm 8.9'$  and  $r_c = 17.9' \pm 2.1'$  for an elliptical galaxy with  $\theta = 49^\circ \pm 1.6^\circ$  and  $\epsilon = 0.54 \pm 0.02$ . The large error bar on the tidal radius is due to the difficulty in fitting a King model to these data. However, our data are most consistent with a large tidal radius due to the continuing steep decline in the surface density seen out to  $\sim 100'$ . This increase in the total extent of Ursa Minor also influences the total luminosity of the system: The total luminosity of the system is directly proportional to the integral of the surface density profile. Based on the King profile fit to Ursa Minor presented here, we estimate that IH95 may have underestimated the total luminosity of Ursa Minor by nearly a factor of  $\sim 2.7$ . The parameters of the King fit (specifically the change in concentration) also affect the mass estimate, but not as significantly as they do the luminosity. Based only on the change in the King profile parameters, we calculate that the standard  $M/L$  value for Ursa Minor should be a factor of 2 smaller than previous estimates, i.e., 47 rather than 95.

It has been argued that no single effect can account for the large inferred  $M/L$  value for Ursa Minor. For example, an anisotropic velocity dispersion may affect the calculation of the virial mass. It may be unlikely that the velocity dispersion of UMi is significantly anisotropic because this would require that the dSph be elongated along the line of

sight, which seems improbable based on its elongation in the plane of the sky and on its narrow horizontal branch. However, if anisotropy is present to some degree in the system’s velocity dispersion, it may only inflate  $M/L$  by a factor of  $\sim 3$  (Richstone & Tremaine 1986); not enough to produce  $M/L \sim 100$  from a system with a true  $M/L \sim 3$ . Although this effect is often discounted since it does not reduce the  $M/L$  of UMi to a value expected for a system with no dark matter, it is worth reconsidering now since anisotropy could reduce  $M/L \sim 47$  to  $M/L \sim 16$ . That is, while we agree that it is unlikely that one single physical effect has inflated the inferred  $M/L$  of Ursa Minor to 100, if several effects, such as underestimating  $L_{tot}$  and the repercussions from an anisotropy of the velocity dispersion each contribute a factor of 2–3 to the measured value of  $M/L$ , it may be that Ursa Minor has a true  $M/L$  that is much less extreme when each of the “minor” effects on  $M/L$  is correctly taken into account. We note that the Leo II dSph, which is located in the distant outer halo and is presumably less affected by the tidal influence of the Galaxy, has  $M/L = 10$  (Mateo 1998).

The discussion presented here concerns the global  $M/L$  ratio for Ursa Minor. An important assumption in the measurement of a global  $M/L$  ratio is that mass follows light, which introduces significant uncertainty into the process because it is not clear that mass follows light in dSph galaxies. For example, Kleyna et al. (2002) present models for the shape of the dark matter halo in the Draco dSph, and they rule out a mass follows light model for that dSph. Because of the uncertainty in the global distribution of dark matter in dSphs, the  $M/L$  ratio in the core is likely to be more robust than the global value. The central  $M/L$  is insensitive to small changes in the total luminosity, such as the one presented here, however the central  $M/L$  is affected by the presence of substructure within the core. Thus, our observations do suggest that both the core and global  $M/L$  ratios in UMi should be reconsidered.

## 5. A NEW MODEL FOR URSA MINOR

The morphology and surface density profile of Ursa Minor derived in previous studies have been used to argue that the stellar system is in the process of losing stars to the Milky Way. Based on accumulated photometric observations, the “standard” model for Ursa Minor is that it is a bound, possibly relaxed elliptical system of  $50'$  major axis tidal radius with “extratidal” stars found at semi-major axis radii  $\gtrsim 50'$  or so. The time to destroy unbound substructure in UMi by phase mixing is roughly 1 Gyr, and thus the presence of substructure within the tidal radius is explained by assuming that the clumps of stars are recent phenomena related to the disruption of the system.

The observations presented here lead us to propose a revision of the standard model of Ursa Minor. We postulate that the primary peak in the surface density is the true core of Ursa Minor, analogous to the suggestion that the “globular cluster” M54 is the nucleus or core of the Sagittarius dwarf (Sarajedini & Layden 1995). Assuming the peak isodensity contours in Figures 12 and 13 define the true core of Ursa Minor, then this suggests that the shape of the outer isodensity contours reflects the tidal shaping of the bound stars around this core and that the true “cen-

ter” of the galaxy need not be the center of symmetry of these outer contours. We note that independent observations that include fainter stars of Ursa Minor not included in our sample (Martínez-Delgado et al. 2002) confirm that the central regions of the dSph contain a dense, globular cluster-like region.

The simplest reason for identifying the offcenter primary density peak seen in the isodensity plot of Ursa Minor as the core of the galaxy is that it is the densest region in the galaxy; all theoretical models of dSph structure (e.g., King models, power-law+core models, CDM halo models, etc.) are constructed so that the highest density is found in the center of the galaxy. In addition to this simple argument, however, there are several other reasons for identifying this structure as the core of the galaxy: (1) Theoretical n-body simulations of dSph galaxies evolving in a tidal field predict that the initially spheroidal satellite becomes more elliptical as distance from the core increases (Johnston et al. 2001). Thus, at late times the simulated dSph still has small ellipticity in the core, but increasing to  $> 0.5$  in the outer regions. The majority of the contours of Ursa Minor in Figure 13 have ellipticity  $> 0.5$ , however, the innermost contours appear more spherical, and are consistent with an ellipticity  $< 0.5$ . (2) The crossing time in Ursa Minor is short,  $\sim 10^7 - 10^8$  years, and therefore substructure within the galaxy is expected to be erased on timescales short compared to the Hubble time. If the core of Ursa Minor is indeed  $> 15'$  in radius (centered between the two density peaks) and is well mixed, then the presence of an offcenter density enhancement is difficult to explain, unless it is a recently formed feature. However, if we identify the highest density peak as the core, then only those stars found within this much smaller region are expected to be well mixed (and the smooth appearance of the contours surrounding this peak suggests this is true) and it is reasonable to expect to see substructure outside of the core, such as the secondary density peak and the twisting of the outer contours. (3) In WF/PC2 images of the core of UMi (centered on the position of highest stellar density from the authors’ earlier ground-based imaging) Battinelli & Demers (1999) find a “ring” of stars; the ring has a central void, surrounded by a circularly symmetric, dense distribution of stars. However, a surface density profile constructed using circular annuli centered at the ring center finds the highest density at a radius of  $\sim 30''$ . This offset is more consistent with the location of the center determined from Figure 13, and, indeed, in the image of chip WF3 in Battinelli & Demers (1999) there is an excess of stars at the edge of the chip near where we predict the center of UMi to be. Moreover, Battinelli & Demers (1999) suggest that the central region of UMi does not follow a King law, but the best fit to their data has a core radius of  $\lesssim 2.5'$ , rather than the  $\sim 15'$  value derived previously.

Identifying the peak in the UMi isodensity contours as the core of the galaxy implies that the core radius is much smaller than previously estimated and also that a larger fraction of the galaxy is susceptible to influence by the Galactic potential than is often supposed. Observations of another stellar system in the Milky Way halo support these conclusions. Recent discovery of extensive tidal tails associated with the globular cluster Pal 5 (Odenkirchen et al. 2001a) provides a system for comparison with Ursa

Minor. Although Pal 5 is a lower mass system than UMi, the behavior of unbound, tidally stripped stars depends on the shape of the Galactic potential and the satellite’s orbit rather than its initial structure (Johnston et al. 2001), so the distribution of the unbound stars around Pal 5 is perhaps reasonable to compare to the extended distribution of UMi stars if they, too, are unbound. Comparing the isodensity contours of Pal 5 (Figure 2 of Odenkirchen et al. 2001a) to those of UMi, there appears to be a similar “S-shaped” morphology in both systems. The bend in the contours of Pal 5 is in the direction of the orbital path of the system, as is the bend in the contours of Ursa Minor. Although this “S-shaped” morphology appears to be related to the tidal disruption of Pal 5 and, by analogy, therefore, to Ursa Minor, it is unclear what is causing this bend. N-body simulations of disrupting systems show that the distribution of particles appears S-shaped because the escaping particles initially leave perpendicular to the orbit (i.e., along the direction of the tidal force), but then bend in the direction of the orbital path as the particles (stars) sort by orbital energy (e.g., Johnston et al. 2001). However, this shape is *in the plane of the orbit*, that is, in order to see it one needs to view the orbit face on. Our line of sight to Ursa Minor is nearly radial, and thus it is unlikely that the S morphology seen in N-body simulations should be visible from our point of view.

In order to test this assumption, we took N-body data from Johnston et al. (2001) and projected the plane containing the particles of the disrupted satellite along the orbital plane of Ursa Minor as determined by the proper motion of Cudworth et al. (2002). As expected, the particles that cause the usual, energy-sorting S morphology in the orbital plane appear linear and symmetric when seen in projection, even after accounting for the Sun’s  $\sim 8$  kpc offset from the Galactic center. Although this suggests that the S-shape derived in N-body simulations is not the source of the twisting seen in the contours of UMi and Pal 5, since the angle between the line of sight to UMi and its orbital plane ( $\sim 25^\circ$ ) is so similar to the angle between the LOS to Pal 5 and its orbital plane ( $\sim 33^\circ$ ), the physics responsible for creating this morphology in Pal 5 may be responsible for the similar morphology seen in UMi. Rotation or tumbling of these two systems may be a viable method for the S-shaped morphology to become visible from our line of sight, however this remains to be investigated.

We note that recent, detailed simulations (M. Odenkirchen 2002, private communication) of the disruption of Pal 5 claim to reproduce the S-shaped morphology of this globular cluster and confirm that it is related to the transition by stars from radial escape to tangential drift parallel to the cluster’s orbit. The results of these simulations show that the bending is largest when viewing the orbital plane face-on, but the projection onto the plane of the observer also shows it clearly, in accordance with the observations.

## 6. SUMMARY AND CONCLUSIONS

Using three color photometry, we have surveyed  $\gtrsim 9$  square degrees in a region centered on the Ursa Minor dwarf spheroidal galaxy. The filters used are designed to allow efficient dwarf/giant luminosity classification of all

stars observed. From among the  $> 14,000$  objects measured that have stellar profiles and small photometric errors, we have selected a sample of 788 candidate Ursa Minor giant stars and 505 candidate Ursa Minor blue horizontal branch stars. A comparison of our catalogue of giants with spectroscopically verified Ursa Minor members and non-members shows that so far we are 100% accurate in separating contaminants and slightly less accurate at recovering all member giants.

Among the candidate UMi stars, many lie beyond the nominal tidal radius of Ursa Minor, as determined by previous studies of the dSph (that assume the King limiting radius is the tidal radius). These “extratidal” RGB stars (which may or may not be bound to the dSph) lie in all directions and are seen to the limits of the surveyed region (up to  $\sim 2.5 - 3.0$  degrees from the center). Due to the intrinsic faintness of the BHB stars, our detection of these stars is incomplete outside of the central survey fields of Ursa Minor. However, even among this incomplete sample of BHB stars we find many extratidal stars, and the spatial distribution of the BHB stars appears almost identical to that of the RGB stars.

Analysis of the spatial distribution of the UMi giant candidates and BHB candidates suggests that Ursa Minor has a peculiar morphology in comparison to the majority of dwarf spheroidals. Unlike most dSphs where the highest density is found at the center of symmetry of the outermost, high signal-to-noise isodensity contours, in UMi, two off-center regions are found to be the areas with the highest stellar density. The western density peak is centrally concentrated and it is less elliptical ( $\epsilon \sim 0.25$ ) than the majority of the galaxy ( $\epsilon = 0.55$ ). The second density peak has been seen by other authors and is not an artifact of the data, but the excess of stars at this location in UMi is of lower significance. The stars that create this peak are not concentrated, but are instead elongated in the direction of the orbital path of UMi. A smoothed representation of the isodensity contours shows that the galaxy has a crescent-shaped, or S-shaped, morphology.

In order to account for the variation in limiting magnitude across the survey region, we divided the candidate UMi RGB stars into three magnitude limited subsamples,  $M_0 \leq 19.3$ ,  $M_0 \leq 19.65$ , and  $M_0 \leq 20.0$ . We derived surface density profiles of Ursa Minor by counting RGB stars in concentric ellipses using the structural parameters of K98. In each case, the resulting profiles look remarkably similar to each other at all radii and to the profile of UMi derived by IH95 for radii  $r < 30'$  or so. The surface density profile is not fit well by previous King profile fits or by our own King profile fit; the densities begin to deviate from the King profile calculated by IH95 perhaps as close as  $6.8'$  to the center, with larger deviations seen at all points  $r > 20.4'$ . There may be a “break” seen in the surface density profile, but it is not as sharp as the one seen in Carina, for example. The points along the surface density profile outside of  $20.4'$  are fit best by a power law with index  $\sim -3$ . Due to the east/west asymmetry seen in the isodensity contours, we derived surface density profiles separately for the eastern and western halves of the dSph. In contrast to the overall profile and that of the western half, the profile of the eastern half of the galaxy does appear to break at  $34.0'$  (similar to IH95), and the

densities past this break follow a more shallow,  $r^{-2}$  power law past this point. The radial profiles derived by IH95 and K98 have high signal-to-noise only for radii  $r < 30'$ , and thus the discrepancy at large radii between the profile presented here and those derived in these previous studies can be attributed to our ability to study UMi at much lower stellar surface densities because we are mostly free from contamination by foreground stars.

Based on the two-dimensional distribution of candidate Ursa Minor stars, we conclude that this system is very likely undergoing significant mass loss due to its tidal interaction with the Milky Way. The morphology of the interior region of the galaxy that is usually considered the core is inconsistent with expectations for a relaxed system. Instead, we propose that the smooth, fairly round density peak west of the “center” of Ursa Minor is the core of the galaxy, and all stars outside this roughly  $2'$  radius region are asymmetrically distributed around this core due to the tidal influence of the Milky Way. Our finding that the  $M/L$  ratio of UMi may be as low as 16 is more consistent with substantial mass loss than previous, large  $M/L$  values. However, we cannot rule out a model in which all of the RGB and BHB stars identified in this study as associated stars are instead bound within an extended, massive dark matter halo. Further investigation of the velocities of the extratidal stars is necessary to determine if they are bound or unbound to the dSph. The photometric survey of Ursa Minor presented here was specifically undertaken in order to identify prime candidates for spectroscopy; a spectroscopic campaign to determine membership and to measure radial velocities for a number of candidate Ursa Minor RGB stars is already underway.

CP wishes to acknowledge the generous support of the University of Virginia Department of Astronomy during the completion of this work, which is a significant portion of his Ph.D. thesis. We note that the referee, Tad Pryor, made numerous suggestions that resulted in a significantly improved manuscript. The authors also wish to acknowledge helpful discussions with Kathryn Johnston and Andrea Schweitzer. This work benefitted from the authors participation in the discussions and debate at the 2001 Ringberg Workshop on The Lowest-Mass Galaxies and Constraints for Dark Matter, organized by Eva Grebel. We wish to acknowledge support for this work from NSF CAREER award AST-9702521, the David and Lucile Packard Foundation, and a Cottrell Scholar Award from the Research Corporation. CP also acknowledges partial support from NSF award AST 00-71223.

## REFERENCES

- Armandroff, T. E., Olszewski, E. W., & Pryor, C. 1995, *AJ*, 110, 2131
- Battinelli, P., & Demers, S. 1999, *AJ*, 117, 1764
- Beers, T. C., Preston, G. W., & Shectman, S. A. 1985, *AJ*, 90, 2089
- Burkert, A. 1997, *ApJ*, 474, L99
- Carney, B. W., Laird, J. B., Latham, D. W., & Aguilar, L. A. 1996, *AJ*, 112, 668
- Chiba, M. & Beers, T. C. 2000, *AJ*, 119, 2843
- Cudworth, K. M., Olszewski, E. W., & Schommer, R. A. 1986, *AJ*, 92, 766
- Cudworth, K. M., Schweitzer, A. E., & Majewski, S. R. 2002, *AJ*, *submitted*
- Demers, S., Battinelli, P., Irwin, M. J., & Kunkel, W. E. 1995, *MNRAS*, 274, 491
- Dinescu, D. I., Majewski, S. R., Girard, T. M., & Cudworth, K. M. 2000, *AJ*, 120, 1892
- Doinidis, S. P., & Beers, T. C. 1989, *ApJ*, 340, L56
- Eggen, O. J., Lynden-Bell, D., & Sandage, A. R. 1962, *ApJ*, 136, 748
- Eskridge, P. B., & Schweitzer, A. E. 2001, *AJ*, 122, 3106
- Fasano, G. & Franceschini, A. 1987, *MNRAS*, 225, 155
- Feltzing, S., Gilmore, G., & Wyse, R. F. G. 1999, *ApJ*, 516, L17
- Flynn, C., Sommer-Larsen, J., Christensen, P. R., & Hawkins, M. R. S. 1995, *A&AS*, 109, 171
- Geisler, D. 1984, *PASP*, 96, 723
- Geisler, D. 1990, *PASP*, 102, 344
- Geisler, D. 1996, *AJ*, 111, 480
- Guhathakurta, P. 2002 *in preparation*
- Hargreaves, J. C., Gilmore, G., & Annan, J. D. 1996, *MNRAS*, 279, 108
- Hargreaves, J. C., Gilmore, G., Irwin, M. J., & Carter, D. 1994, *MNRAS*, 271, 693
- Harris, W. E., Fitzgerald, M. P. & Reed, B. C. 1981, *PASP*, 93, 507
- Helmi, A., & White, S. D. M. 1999, *MNRAS*, 307, 495
- Hodge, P. W., & Michie, R. W. 1969, *AJ*, 74, 587
- Ibata, R., Gilmore, G., & Irwin, M. 1994, *Nature*, 370, 194
- Ibata, R., Gilmore, G., & Irwin, M. 1995, *MNRAS*, 277, 781
- Ibata, R., Irwin, M., Lewis, G. F., & Stolte, A. 2001a, *ApJ*, 547, L133
- Ibata, R., Lewis, G. F., Irwin, M., Totten, E., & Quinn, T. 2001b, *ApJ*, 551, 294
- Irwin, M. 1998, in *IAU Symposium 192, The Stellar Content of Local Group Galaxies*, ed. P. Whitelock & R. Cannon (San Francisco: ASP), 29
- Irwin, M. J., & Hatzidimitriou, D. 1993, in *The Globular Cluster-Galaxy Connection*, ed. G. Smith & J. Brodie (San Francisco: ASP), 322
- Irwin, M., & Hatzidimitriou, D. 1995, *MNRAS*, 277, 1354 (IH95)
- Ivezić, Željko et al. 2000, *AJ*, 120, 963
- Johnston, K. V., Choi, P., & Guhathakurta, P. 2002, *AJ*, 124, 127
- Johnston, K. V., Hernquist, L., & Bolte, M. 1996, *ApJ*, 465, 278
- Johnston, K. V., Sigurdsson, S., & Hernquist, L. 1999, *MNRAS*, 302, 771
- King, I. R. 1962, *AJ*, 67, 471
- Klessen, R. S., & Kroupa, P. 1998, *ApJ*, 498, 143
- Kleyna, J. T., Geller, M. J., Kenyon, S. J., Kurtz, M. J., & Thorstensen, J. R. 1998, *AJ*, 115, 2359 (K98)
- Kleyna, J., Wilkinson, M. I., Evans, N. W., Gilmore, G., & Frayn, C. 2002, *MNRAS*, 330, 792
- Kocevski, D. D. & Kuhn, J. R. 2000, *BAAS*, 197, 30.04.
- Kuhn, J. R., & Miller, R. H. 1989, *ApJ*, 341, L41
- Kuhn, J. R., Smith, H. A., & Hawley, S. L. 1996, *ApJ*, 469, L93
- Kunkel, W. E., & Demers, S., 1976, *Roy. Green. Obs. Bull.* 182, 241
- Larsen, J. A. & Humphreys, R. M. 1994, *ApJ*, 436, L149
- Lynden-Bell, D. 1982a, *Observatory*, 102, 7
- Lynden-Bell, D. 1982b, *Observatory*, 102, 202
- Lynden-Bell, D. & Lynden-Bell, R. M. 1995, *MNRAS*, 275, 429 (LB<sup>2</sup>95)
- Majewski, S. R. 1992a, *ApJS*, 78, 87
- Majewski, S. R. 1992b, in *IAU Symposium 149: The Stellar Populations of Galaxies*, ed. B. Barbuy & A. Renzini, (Dordrecht: Kluwer), 61
- Majewski, S. R., Munn, J. A., & Hawley, S. L. 1994, *ApJ*, 427, L37
- Majewski, S. R., Munn, J. A., & Hawley, S. L. 1996, *ApJ*, 459, L73
- Majewski, S. R., Ostheimer, J. C., Kunkel, W. E., & Patterson, R. J. 2000a, *AJ*, 120, 2550
- Majewski, S. R., Ostheimer, J. C., Patterson, R. J., Kunkel, W. E., Johnston, K. V., & Geisler, D. 2000b, *AJ*, 119, 760
- Majewski, S. R., Phelps, R. & Rich, R. M. 1996, in *The History of the Milky Way and Its Satellite System*, ed. A. Burkert, D. Hartmann, & S. Majewski, (San Francisco: ASP), 1
- Majewski, S. R., Siegel, M. H., Kunkel, W. E., Reid, I. N., Johnston, K. V., Thompson, I. B., Landolt, A. U., & Palma, C. 1999, *AJ*, 118, 1709
- Martínez-Delgado, D., Alonso-García, J., Aparicio, A., & Gómez-Flechoso, M. A. 2001, *ApJ*, 549, L63
- Martínez-Delgado, D., Gómez-Flechoso, M. A., Aparicio, A., & Alonso-García, J. 2002, *in preparation*
- Mateo, M., Olszewski, E. W., & Morrison, H. L. 1998, *ApJ*, 508, L55
- Mateo, M. 1998, *ARA&A*, 36, 435
- McGlynn, T. A. 1990, *ApJ*, 348, 515
- Mighell, K. J., & Burke, C. J. 1999, *AJ*, 118, 366
- Monet, D. et al. 1998, *USNO-A V2.0 A Catalog of Astrometric Standards*, (Annapolis: USNO)
- Moore, B., & Davis, M. 1994, *MNRAS*, 270, 209
- Morrison, H. L., Olszewski, E. W., Mateo, M., Norris, J. E., Harding, P., Dohm-Palmer, R. C., & Freeman, K. C. 2001, *AJ*, 121, 283
- Newberg, H. J. et al. 2002, *ApJ*, 569, 245.
- Odenkirchen, M. et al. 2001a, *ApJ*, 548, L165
- Odenkirchen, M. et al. 2001b, *AJ*, 122, 2538
- Oh, K. S., Lin, D. N. C., & Aarseth, S. J. 1995, *ApJ*, 442, 142
- Olszewski, E. W. & Aaronson, M. 1985, *AJ*, 90, 2221
- Olszewski, E. W., Pryor, C., & Armandroff, T. E. 1996, *AJ*, 111, 750
- Ostheimer, J. C. 2002, Ph.D. Thesis, University of Virginia
- Palma, C., Link, R., Majewski, S. R., Ostheimer, J. C., Frinchaboy, P. M., Patterson, R. J., Kunkel, W. E., Johnston, K. V., & Geisler, D. 2002, *AJ*, *in preparation*
- Palma, C., Majewski, S. R., & Johnston, K. V. 2002, *ApJ*, 564, 736
- Paltoglou, G., & Bell, R. A. 1994, *MNRAS*, 268, 793
- Piatek, S., & Pryor, C. 1995, *AJ*, 109, 1071
- Piatek, S., Pryor, C., Armandroff, T. E., & Olszewski, E. W. 2001, *AJ*, 121, 841
- Press, W. H., Teukolsky, S. A., Vetterling, W. T., & Flannery, B. P. 1992, *Numerical Recipes in Fortran* (2d ed.; Cambridge: Cambridge University Press)
- Preston, G. W., Shectman, S. A., & Beers, T. C. 1991, *ApJ*, 375, 121
- Pryor, C. 1996, in *The Formation of the Galactic Halo... Inside and Out*, ed. H. Morrison & A. Sarajedini, (San Francisco: ASP), 424
- Richstone, D. O. & Tremaine, S. 1986, *AJ*, 92, 72
- Sarajedini, A. & Layden, A. C. 1995, *AJ*, 109, 1086
- Schlegel, D. J., Finkbeiner, D. P., & Davis, M. 1998, *ApJ*, 500, 525
- Searle, L., & Zinn, R. 1978, *ApJ*, 225, 357
- Shetrone, M. D., Côté, P., & Sargent, W. L. W. 2001, *ApJ*, 548, 592
- Siegel, M., Majewski, S., & Patterson, R. 2000, *BAAS*, 197, 113.402
- Siegel, M. H. 2001, Ph.D. Thesis, University of Virginia
- Sommer-Larsen, J., & Zhen, C. 1990, *MNRAS*, 242, 10
- Unavane, M., Wyse, R. F. G., & Gilmore, G. 1996, *MNRAS*, 278, 727
- Wilhelm, R., Beers, T. C., Sommer-Larsen, J., Pier, J. R., Layden, A. C., Flynn, C., Rossi, S., & Christensen, P. R. 1999, *AJ*, 117, 2329
- Yanny, B. et al. 2000, *ApJ*, 540, 825.
- York, D. G. et al. 2000, *AJ*, 120, 1579.



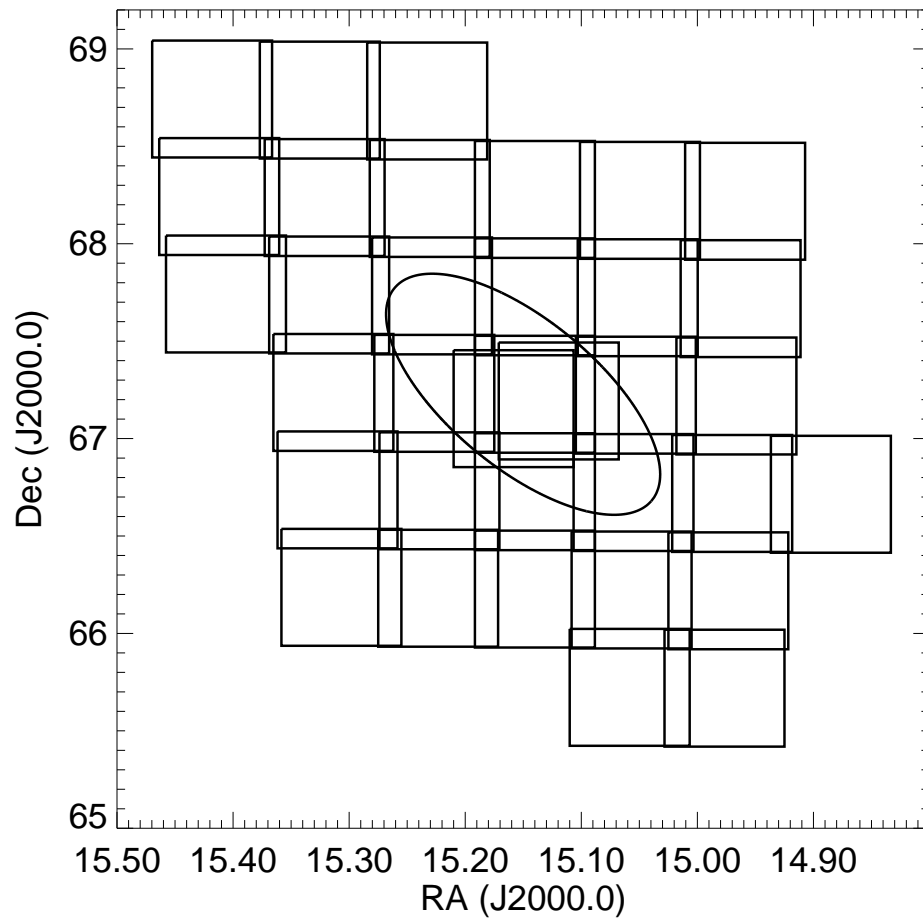


FIG. 1.— The grid of Mosaic frames observed around Ursa Minor. Three overlapping frames with longer exposure times were taken of the core of the galaxy. Surrounding the core fields, an array of 32 additional frames were observed with shorter exposure times. The approximate tidal radius of Ursa Minor is shown as an ellipse for reference.

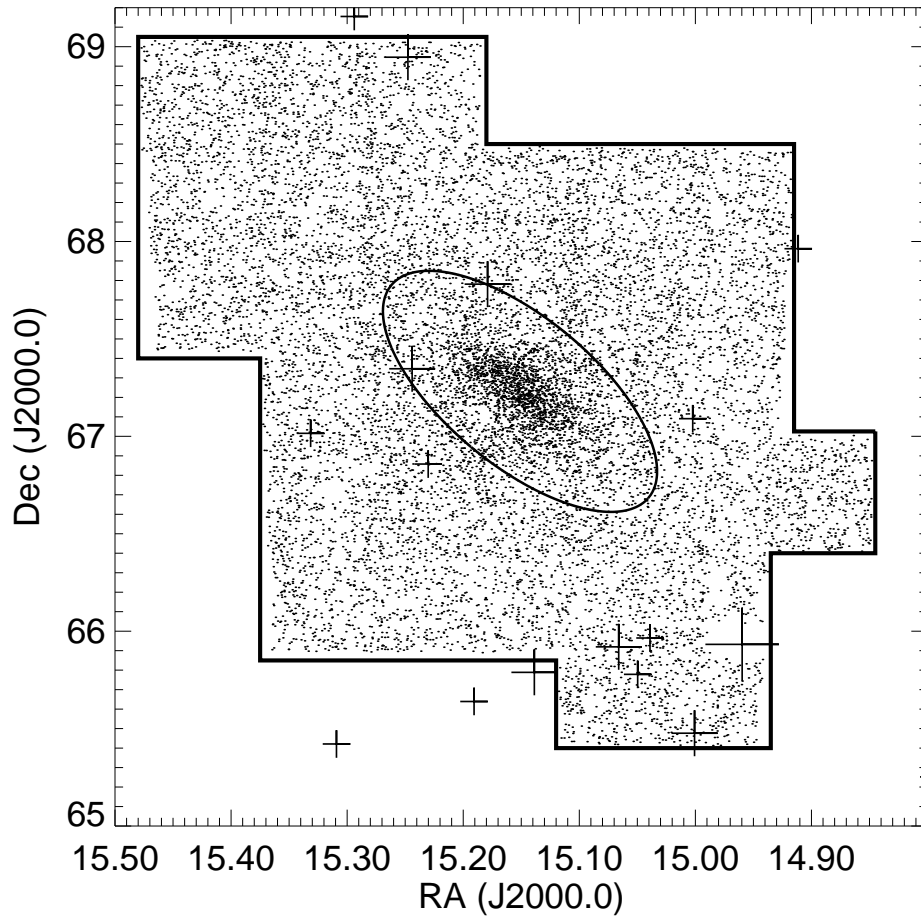


FIG. 2.— Map of all stars detected in the survey region, which is centered on Ursa Minor. All fields observed during this program were taken under photometric conditions. The solid line gives a rough indication of the boundaries of the survey. The ellipse represents the shape of Ursa Minor derived from the shallow data of K98. The semi-major axis is set at the  $\sim 51'$  tidal radius (IH95), which may or may not agree with the value derived by K98 (see §4.2). The crosses mark the locations of the brightest stars found in our survey region. The largest cross marks the location of the  $V = 4.7$  magnitude variable star RR UMi, which saturated almost an entire chip of the Mosaic camera. The slightly smaller crosses mark the locations of stars with  $5 < V < 7$ , while the smallest crosses mark the locations of stars with  $7 < V < 8$ . The combination of the bright stars along the southern edge of the survey and bright moonlight created a gradient in the limiting magnitude of the survey across the grid.

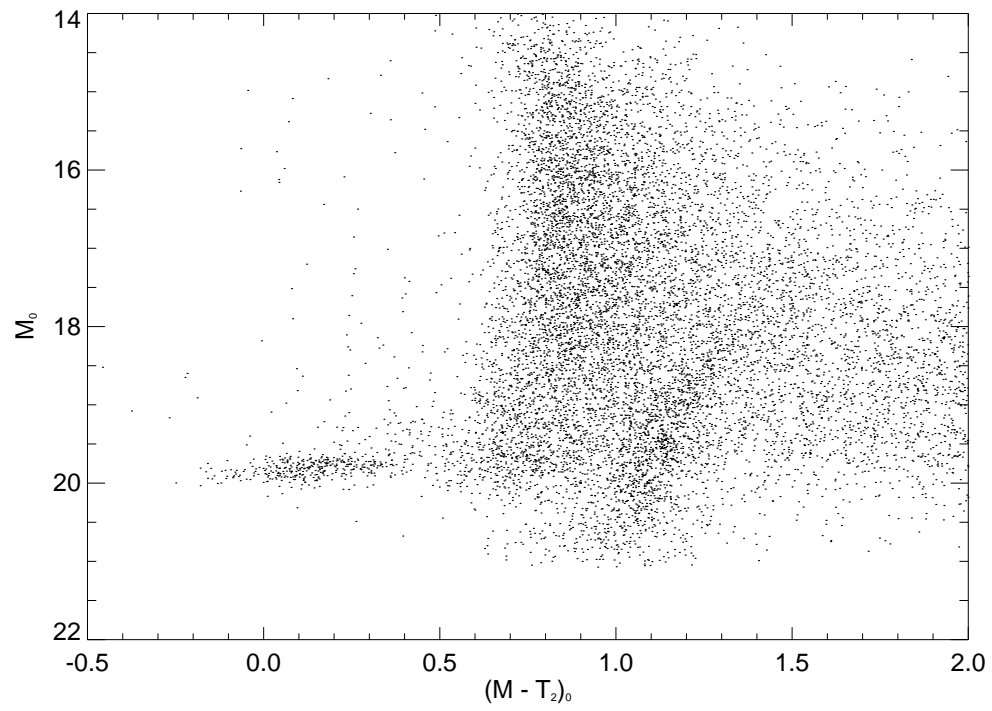


FIG. 3.— Dereddened  $(M - T_2, M)_0$  color-magnitude diagram for all stellar objects found in our survey area. Only objects with stellar profiles and with magnitude errors  $< 0.1$  in all three filters are included.

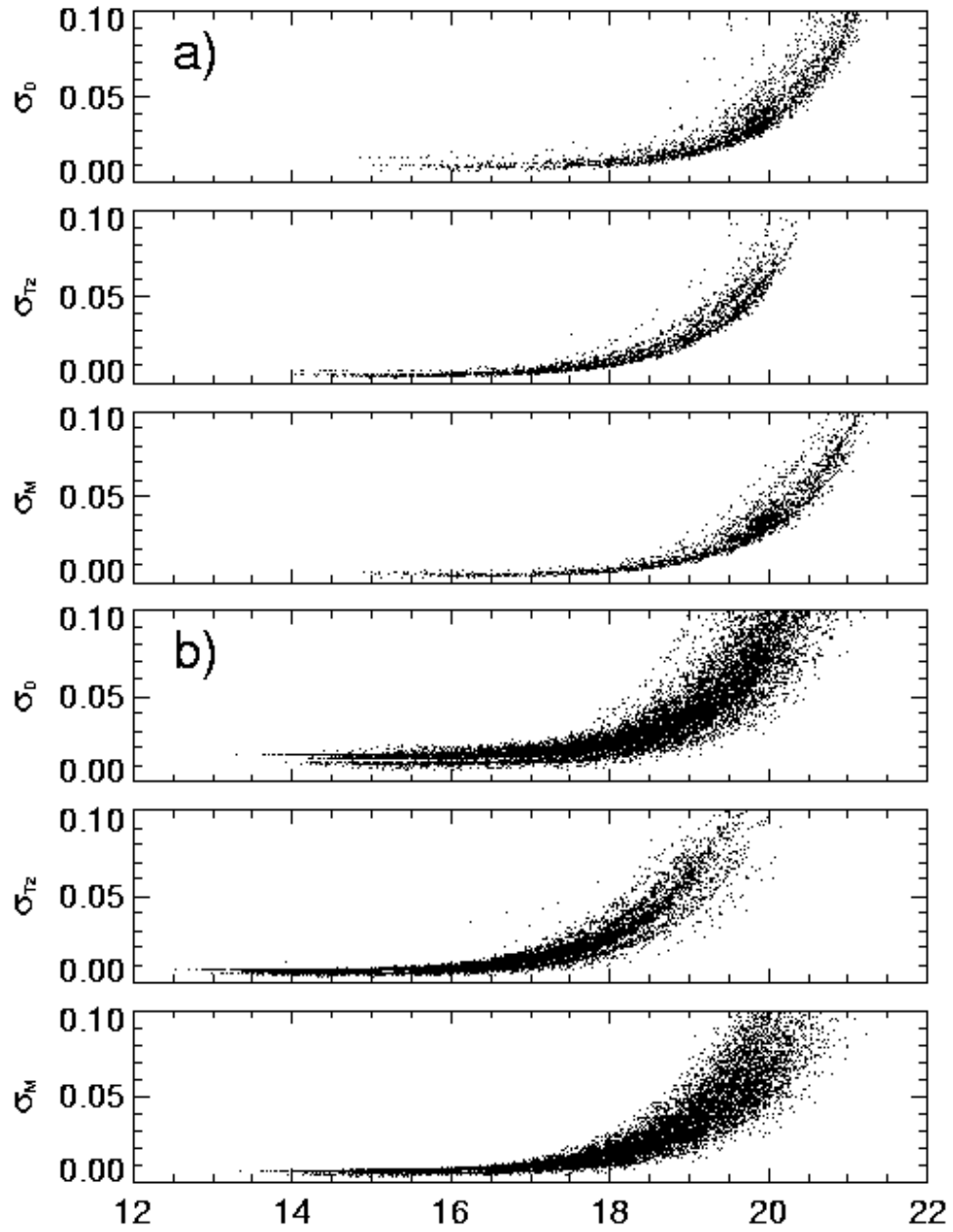


FIG. 4.— Photometric errors for stellar objects in the survey region as a function of magnitude for the (a) core fields and (b) surrounding fields.

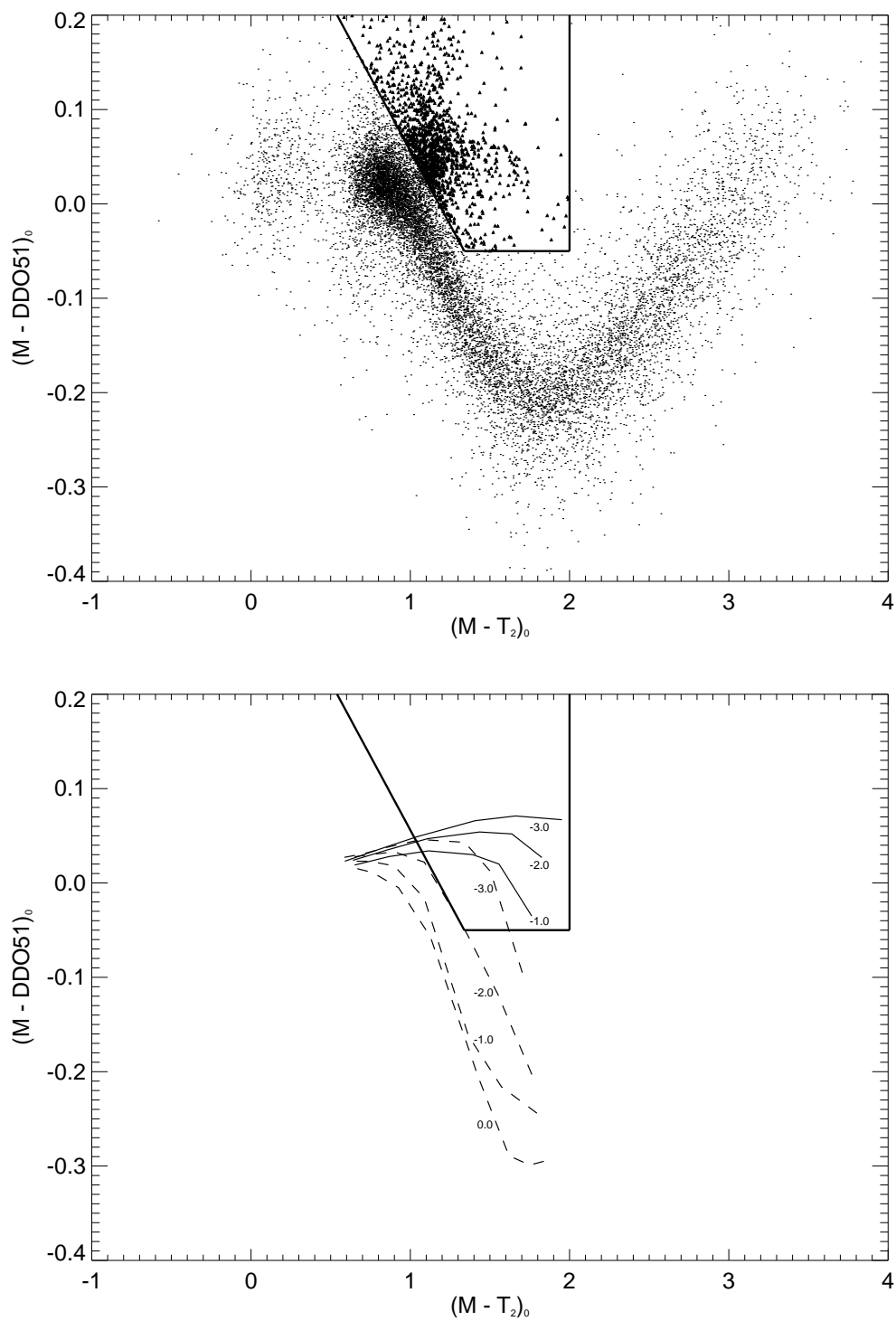


FIG. 5.— The top panel is the  $(M - T_2, M - DDO51)_0$  color-color diagram for stars shown in Figure 3. Dwarf stars lie along the prominent, elbow-shaped locus in the diagram. Giant stars (plotted as filled triangles) lie predominantly in the region bounded by the solid line seen in both panels. The expected isochrones for dwarfs and giants of specific metallicities (derived from synthetic spectra of Paltoglou & Bell 1994) are shown as dashed and solid lines respectively in the lower panel.

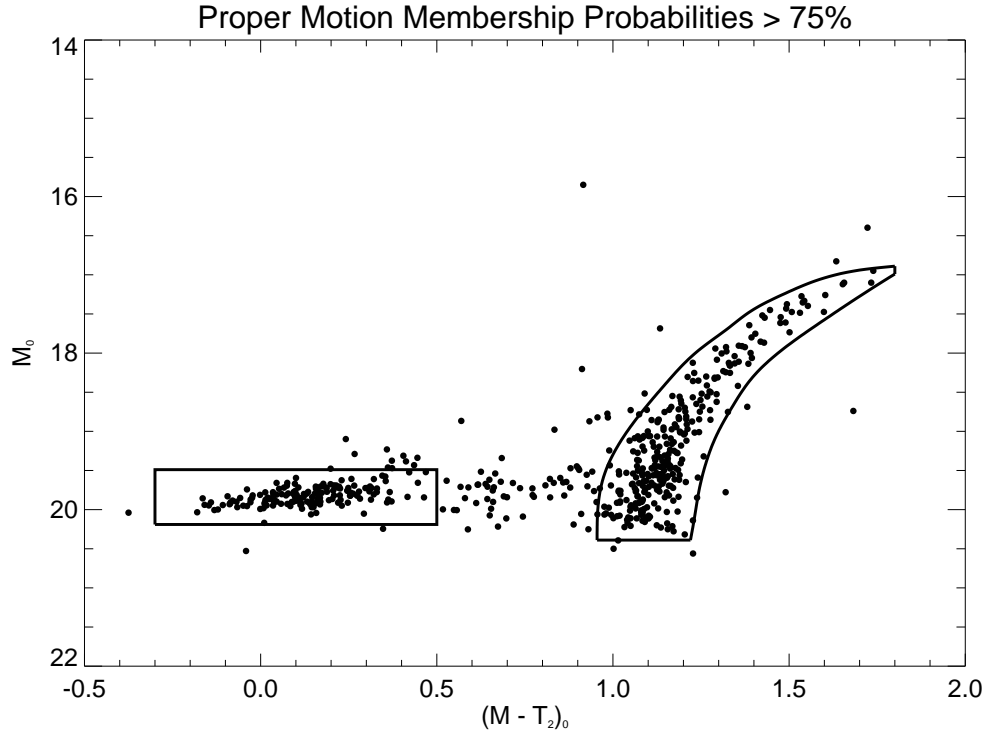


FIG. 6.—  $(M - T_2, M)_0$  color-magnitude diagram for those stars in our catalogue that also have proper motion membership probabilities  $> 75\%$  in the Cudworth et al. (2002) catalogue. The adopted RGB locus for Ursa Minor is designed to contain most of these proper motion-selected giants while limiting contamination from field giants. Blue Horizontal Branch stars are also easily visible in this diagram, and we draw a BHB bounding box useful for selecting these stars over the entire survey region, as well. We discuss the BHB selection in §3.6

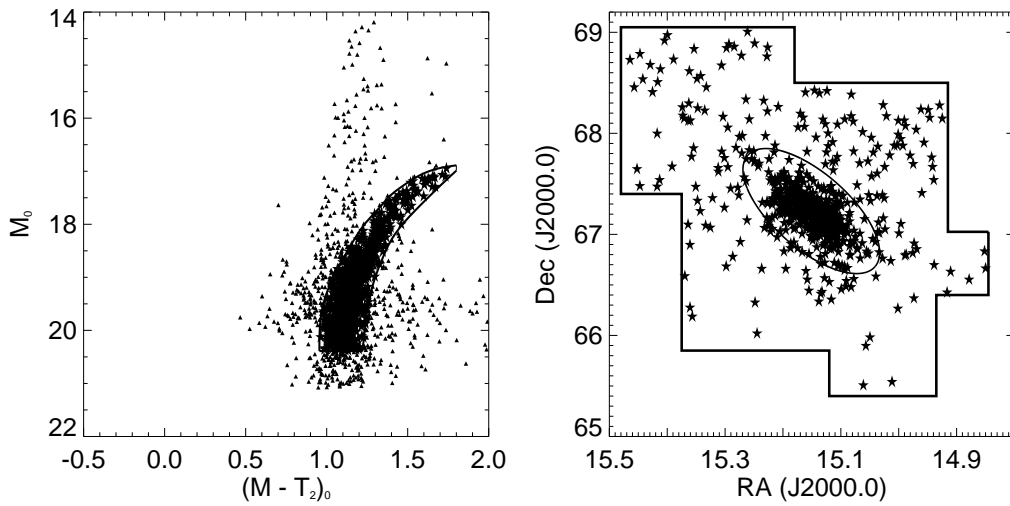


FIG. 7.— Selection of candidate Ursa Minor giant stars. The left panel is the CMD for stars selected to be giants in our catalogue; triangles represent those stars selected as giant stars with the color-color cut from Figure 5, while those giants that also lie in the Ursa Minor RGB region of the CMD are plotted as stars. The right panel shows the distribution of the Ursa Minor giant candidates on the sky. As in Figure 2, the ellipse represents the previous measurements of Ursa Minor's shape and tidal radius. The relative paucity of stars at southern declinations is a reflection of the variation in limiting magnitude across our survey area; the southwestern fields have the brightest limiting magnitudes, and thus we detect fewer giants in this region.

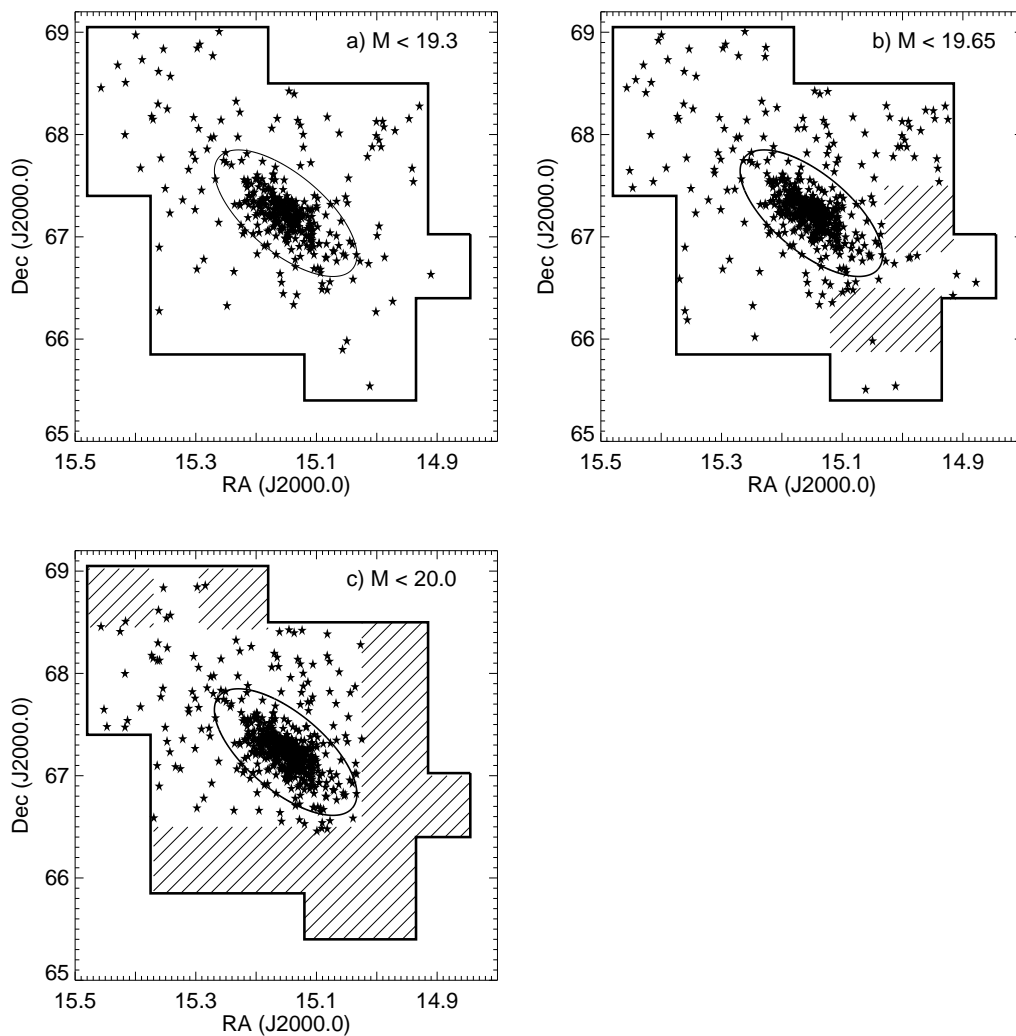


FIG. 8.— Three magnitude limited subsamples of Ursa Minor giant candidates. Panel a (upper left) is the  $M_0 \leq 19.3$  sample, panel b (upper right) is the  $M_0 \leq 19.65$  sample, and panel c (lower left) is the  $M_0 \leq 20.0$  sample. The hatched areas in the two fainter subsamples represent area excluded from the sample because those frames were incomplete at the magnitude limit of the sample. The stars plotted within hatched regions in the panels were detected on adjoining frames (all of our frames overlap by  $5'$ ).

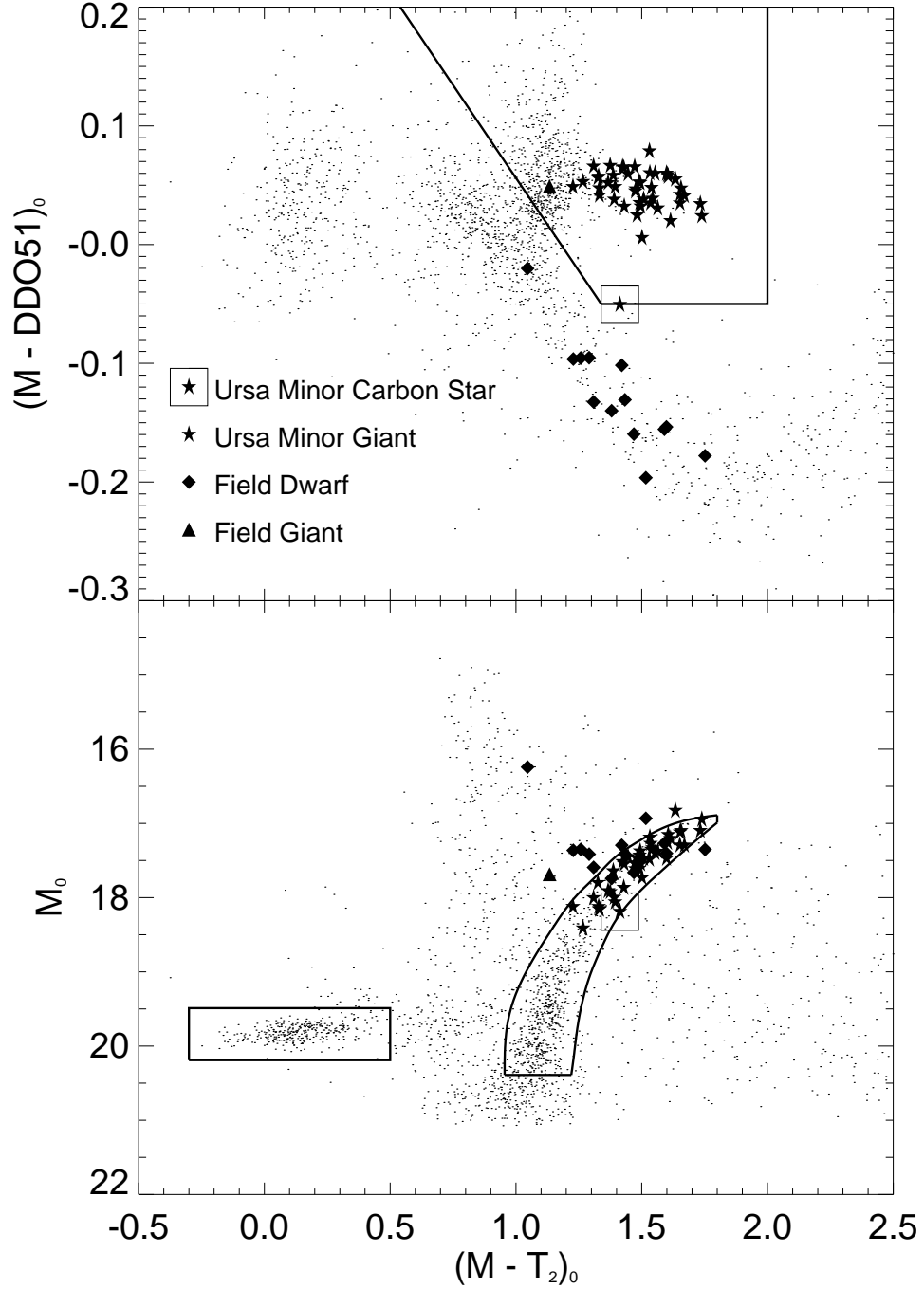


FIG. 9.— The positions of spectroscopically verified Ursa Minor stars and spectroscopically verified contaminants from the Hargreaves et al. (1994) catalogue in color-color (upper panel) and color-magnitude (lower panel) space. In the color-color diagram, the giants (filled triangle and filled stars) and dwarfs (filled diamonds) separate cleanly. All of the dwarfs are found outside of our giant selection region, but the halo K-giant is found inside of the giant region. The carbon star in the catalogue (CUD122 in the catalogue of Hargreaves et al. 1994) is found near the edge of the giant selection region in color-color space. All except one (EDO26 in the catalogue of Hargreaves et al. 1994) of the spectroscopically verified Ursa Minor giant candidates lie inside our RGB bounding box in the CMD. We speculate that this star may be an AGB star or other type of post-RGB star. The field halo K-giant lies well outside of the CMD RGB box but was successfully classified as a giant.



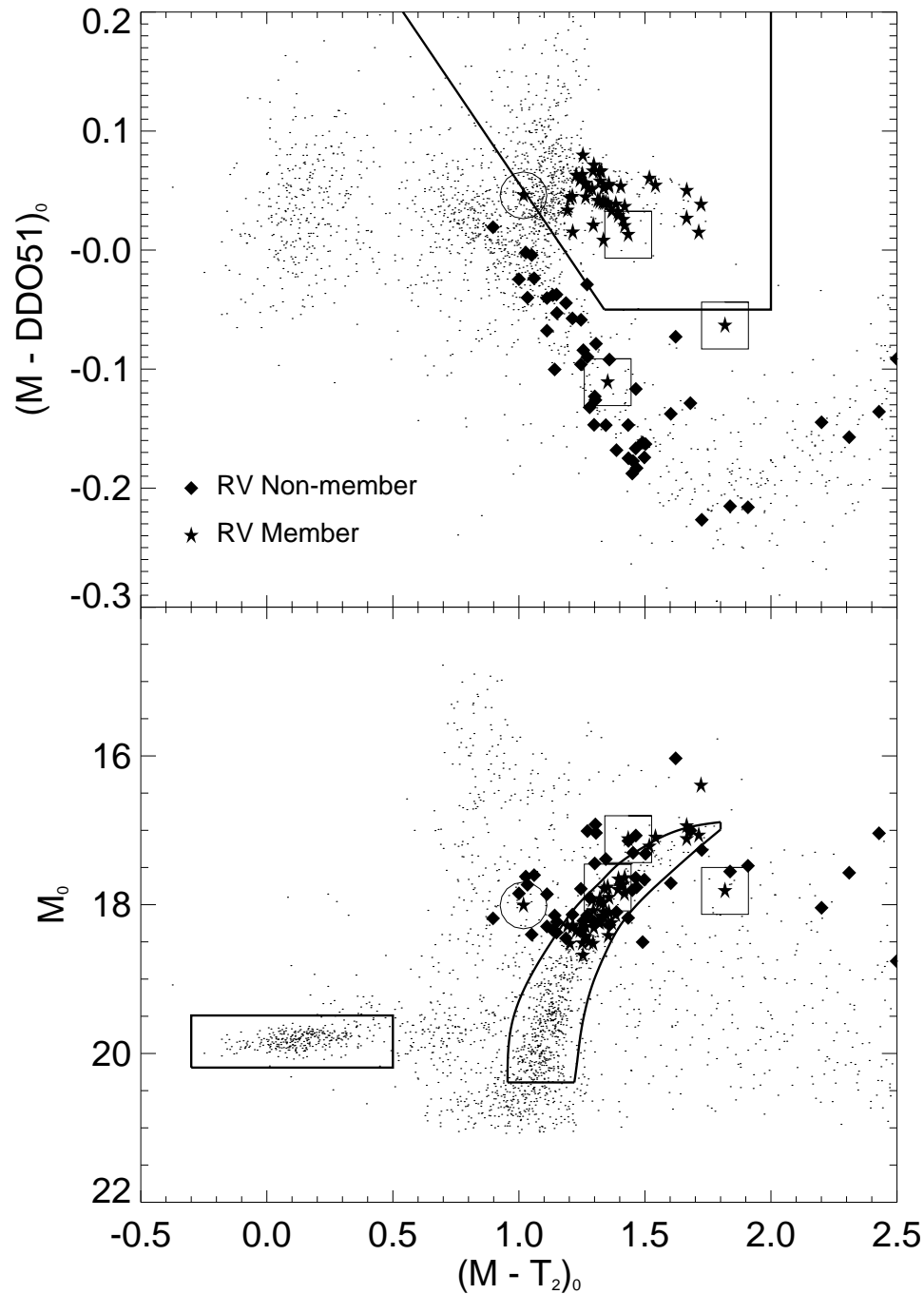


FIG. 10.— The positions of spectroscopically verified Ursa Minor stars and spectroscopically verified contaminants from the Armandroff et al. (1995) catalogue (and not already shown in Figure 9) in color-color (upper panel) and color-magnitude (lower panel) space. As in Figure 9, the contaminants present in the Armandroff et al. (1995) catalogue appear to be entirely disk dwarfs, but in our study, these stars separate cleanly from the color-color selected giants in the color-color diagram. Several of the stars identified as Ursa Minor members by their radial velocity fail one or both of our UMi giant selection criteria. One of these stars, N98, is circled. This star has a velocity  $\sim 50 \text{ km s}^{-1}$  from the systemic velocity of UMi, and is only considered a possible member by Armandroff et al. (1995). Our photometry suggests it is a non-member. Several of the other radial velocity members that fail our giant selection criteria are known carbon stars; these three stars are enclosed in open squares. The other radial velocity members that fail our giant selection criteria may be AGB stars, which our RGB selection region was not designed to include.

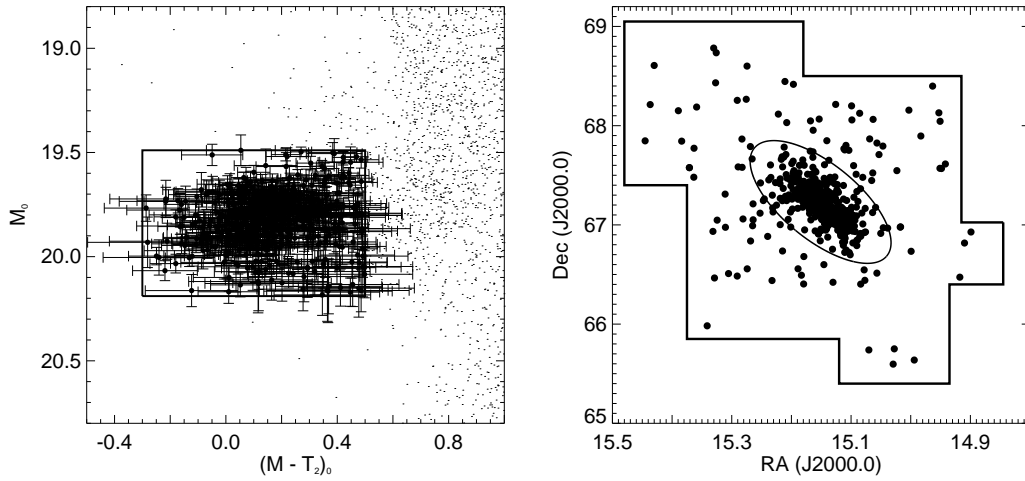


FIG. 11.— Blue horizontal branch (BHB) stars in our Ursa Minor catalogue. The left panel is the  $(M - T_2, M)_0$  CMD of the region in color-magnitude space that includes Ursa Minor BHB stars. The bounding box used to select candidate BHB stars shown in Figure 6 is reproduced here. Also, each star is shown with its error bars in both dimensions. The right panel is the spatial distribution of the Ursa Minor BHB candidates. The region that appears devoid of BHB stars is due to the variation of limiting magnitude among the various grid fields; several grid fields do not go deep enough to detect any BHB stars.

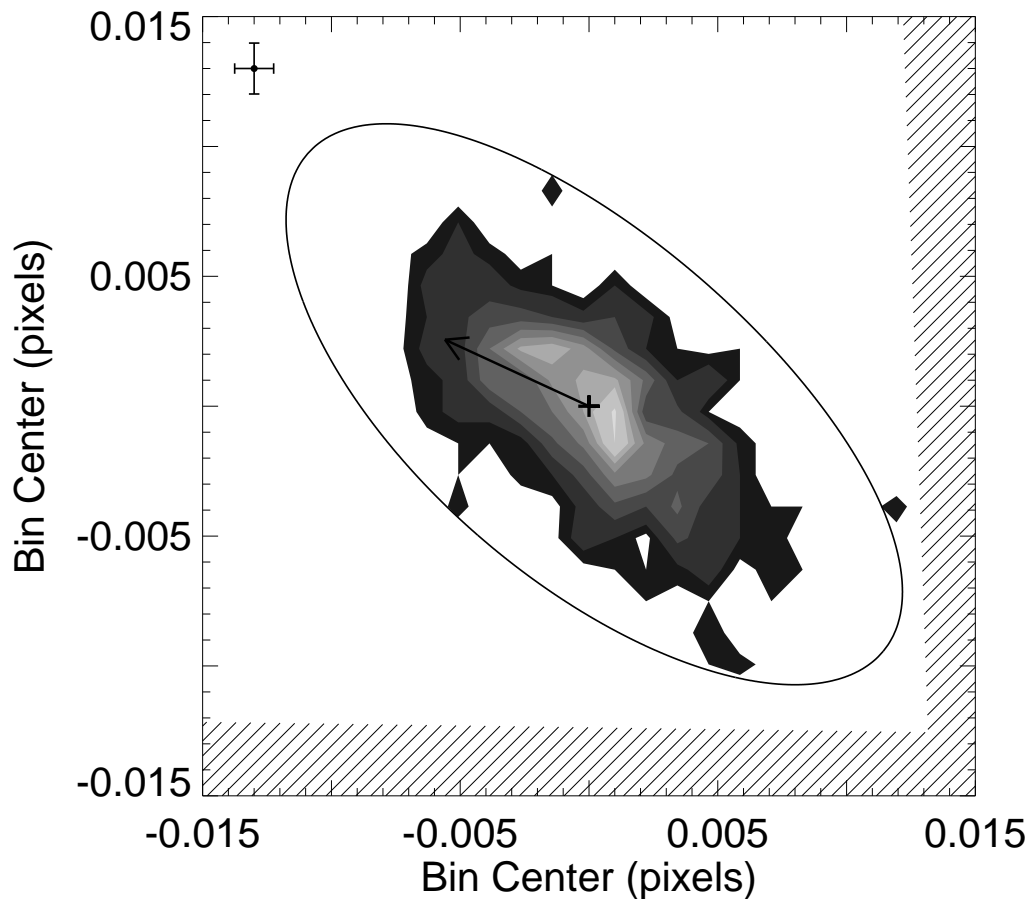


FIG. 12.— Isodensity contours of Ursa Minor. A sample of 1001 candidate Ursa Minor RGB and BHB stars are represented by this image. The hatched region (reproduced from Figure 8) indicates area within our survey region excluded from this analysis due to incompleteness problems. The equatorial coordinates of each RGB and BHB star were converted to Cartesian using a tangential projection (the image is presented such that north is up and east is to the left). The Cartesian space was divided into a grid of  $50 \times 50$  “pixels” of equal area ( $\sim 17.5$  square arcminutes), and stars were counted in each grid cell. This figure represents the inner  $25 \times 25$  pixels in the grid, and is 1.7 degrees on a side. The contour levels are 2,4,8,12,16,20,24,27,33,34 stars per pixel. The adopted center (K98) of Ursa Minor used in the projection is plotted as a cross. The direction of the orbit of UMi based on the Cudworth et al. (2002) proper motion is indicated as an arrow. The error bars plotted in the upper left corner represent the uncertainty in the location of the end of the arrow calculated from the proper motion. Several features are visible in the contours: There do appear to be two off-center peaks separated by a valley. The secondary peak is elongated in a direction between the major and minor axes. Thus, the overall central morphology of Ursa Minor appears to be crescent shaped or hooked, rather than elliptical.

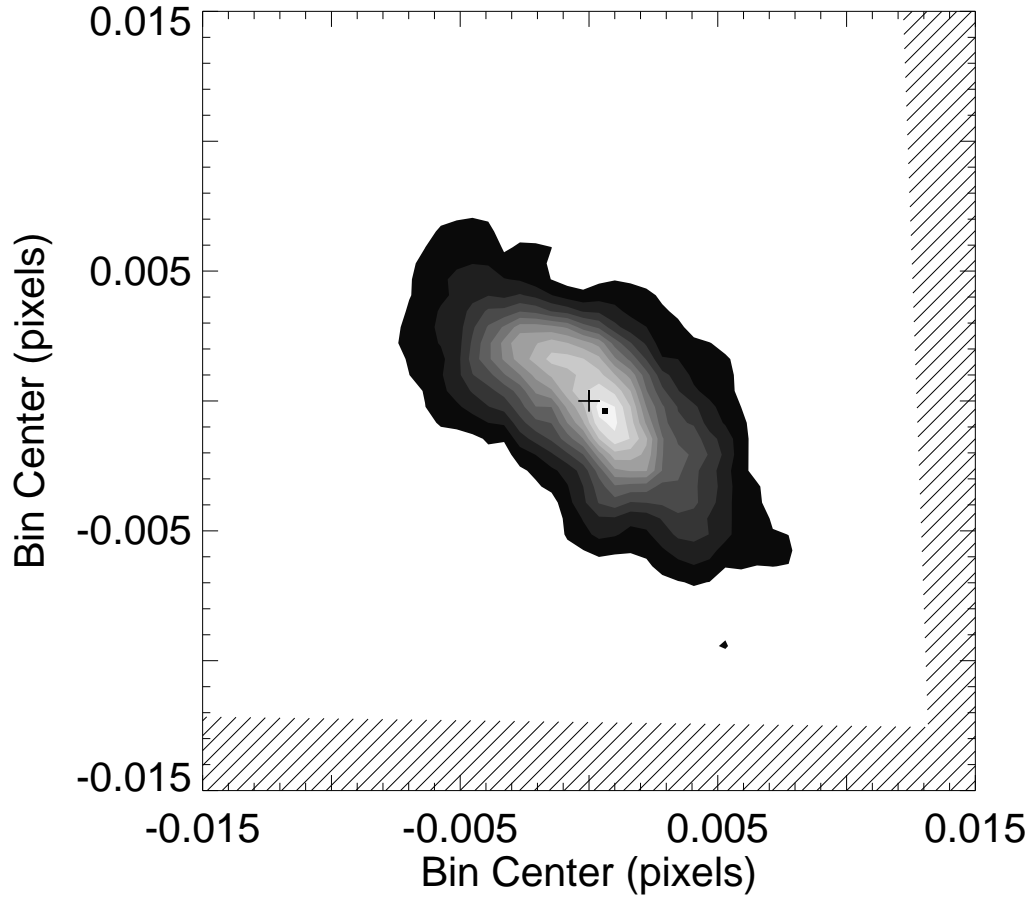


FIG. 13.— Smoothed isodensity contours of Ursa Minor. The single points at each stellar position that were gridded to create Figure 12 were replaced by two dimensional Gaussians centered at the stellar position. The “smoothed” stars were rebinned using a finer,  $100 \times 100$  pixel grid. The counts in each pixel are represented as a contour plot here. The K98 center is represented by the cross. The center of symmetry of the “ring” of UMi stars seen in the HST images of Battinelli & Demers (1999) is plotted as a filled square. Note that this square is slightly offset to the northeast of the densest region of Ursa Minor in the image presented here.

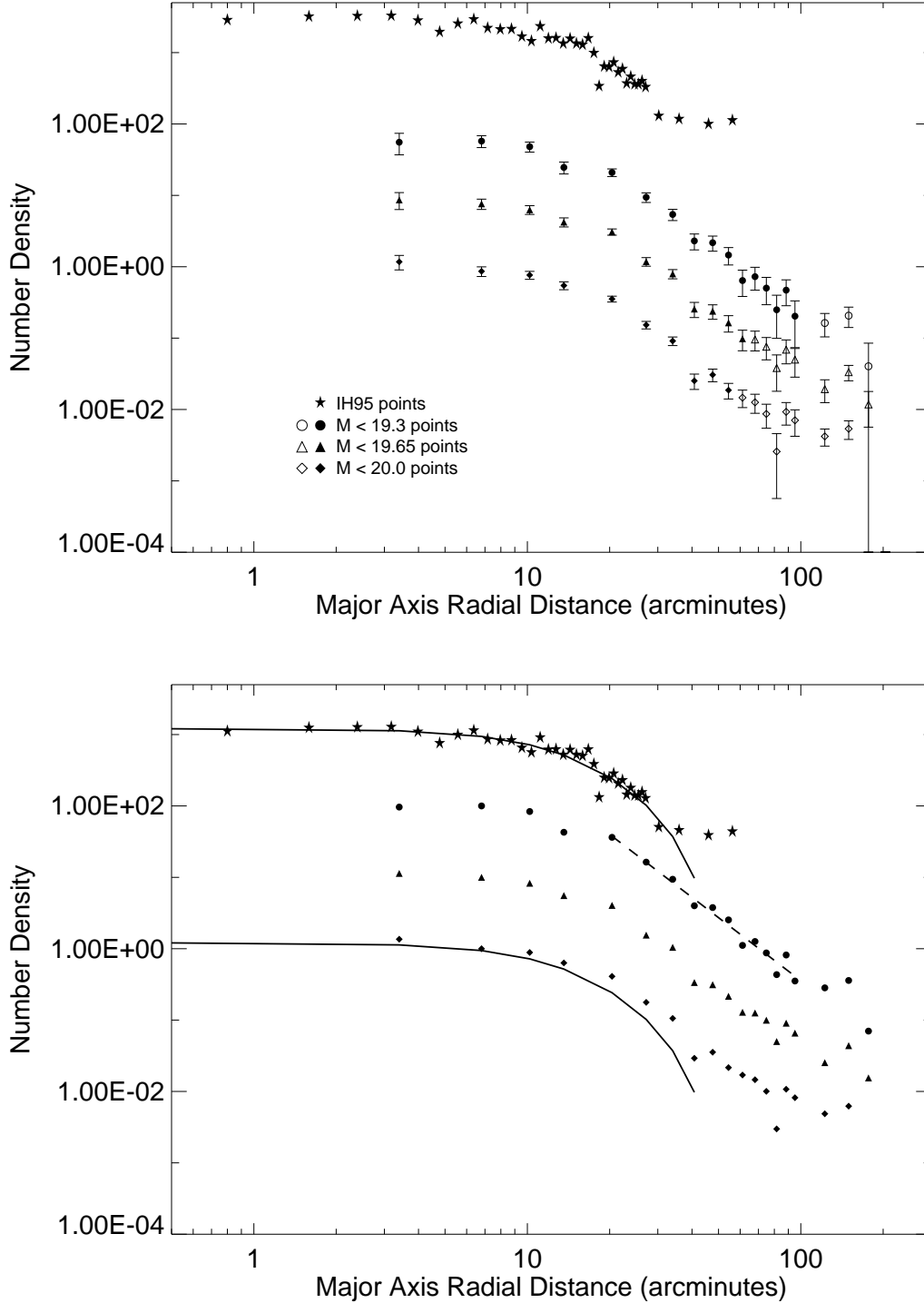


FIG. 14.— Radial surface density profile of Ursa Minor. In both panels, the points have been offset vertically by a factor of 10 for ease of comparison. The upper panel represents the background subtracted stellar densities in  $\text{arcmin}^{-2}$  for the three magnitude-limited samples of giant candidates presented in Figure 7: The filled circles represent  $M_0 \leq 19.3$  giants, the filled triangles represent  $M_0 \leq 19.65$  giants, and the filled diamonds represent the  $M_0 \leq 20.0$  giants. The open symbols for each sample correspond to those annuli that extend beyond the boundaries of our survey region and are therefore not completely sampled. The filled stars are the background subtracted densities from the Ursa Minor star counts of IH95. The densities have been normalized to 1.0 at  $R \sim 6.8'$ . The solid line is the King profile fit to the data by IH95, with  $r_t = 50.6'$  and  $r_c = 15.8'$ . The dashed line is a power law with index  $\gamma = 3$  fit to the filled circles at radii  $\geq 20.4'$ .

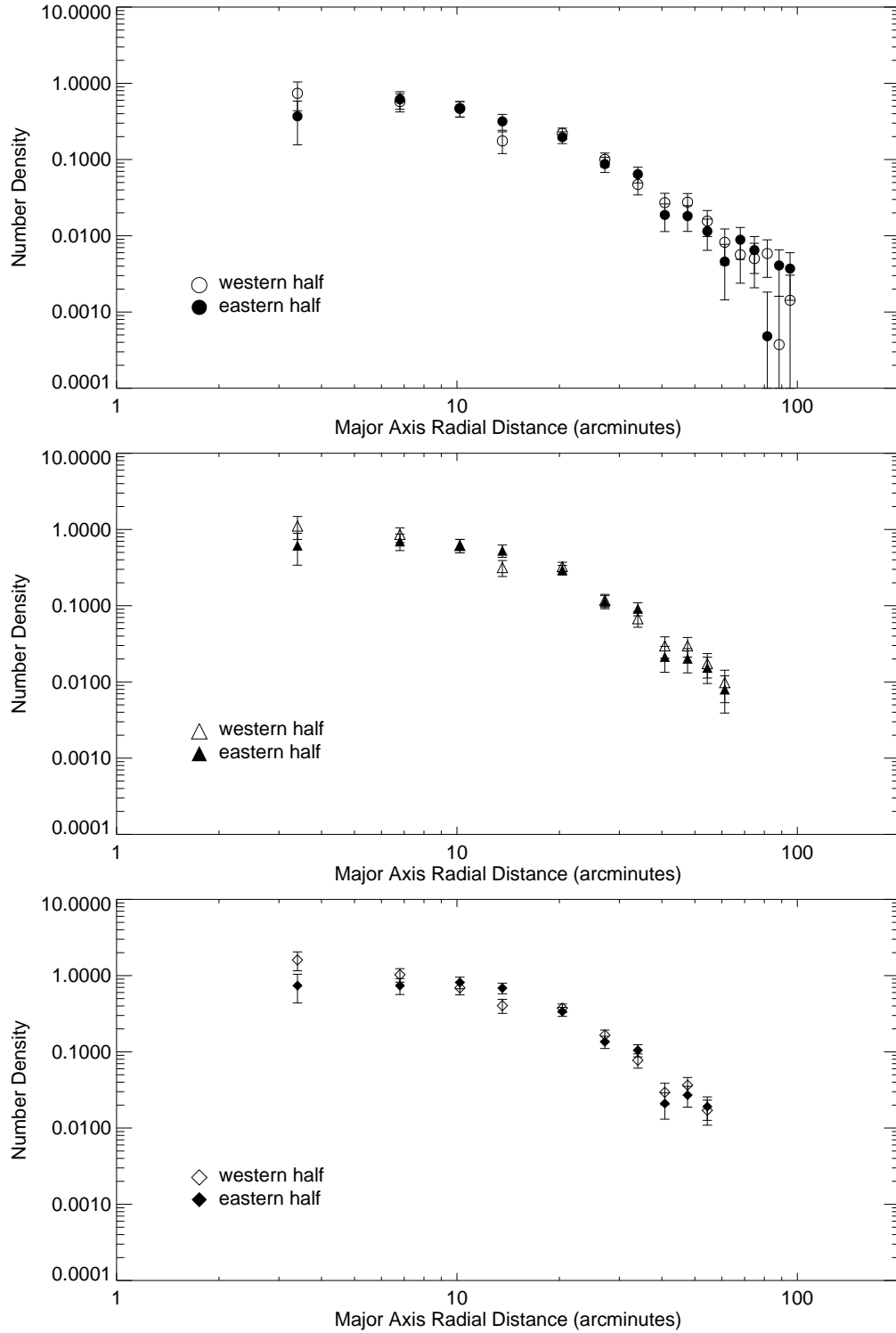


FIG. 15.— Radial surface density profiles for eastern and western halves of Ursa Minor. In each panel, the open symbols represent the number density of stars found in semi-ellipses west of the minor axis, while the filled symbols represent the number density of stars found in semi-ellipses east of the minor axis. The upper panel (circles) is the profile of the  $M_0 \leq 19.3$  sample of UMi giant star candidates, the middle panel (triangles) the  $M_0 \leq 19.65$  sample, and the lower panel (diamonds) is the  $M_0 \leq 20.0$  sample. Although the eastern and western profiles are generally similar, two effects are seen: Due to the presence of the density peak in the western half of the galaxy, the central density is enhanced and the subsequent decline is steeper in the core region of the western profile than it is in the eastern profile. Also, the western profile decays with a  $\Sigma(r) \sim r^{-3}$  power law outside the core region, while the eastern profile shows a break in the profile at  $r = 34.0'$ , followed by a shallower  $\Sigma(r) \sim r^{-2}$  power law decay past the break point.

TABLE 1  
UMI CANDIDATE RGB AND BHB STAR PHOTOMETRY<sup>a</sup>

ID	$\alpha^b$	$\delta^b$	$M$	$\sigma_M$	$T_2$	$\sigma_{T_2}$	$DDO51$	$\sigma_{DDO51}$	Type
15	15:11:45.13	67:21:45.4	19.80	0.03	18.63	0.02	19.71	0.03	rgb
32088	15:10:17.65	67:20:15.4	18.40	0.01	17.16	0.01	18.37	0.02	rgb
1800035	15:09:18.40	66:26:32.3	18.45	0.02	17.15	0.01	18.41	0.02	rgb
7	15:11:51.56	67:26:46.9	19.85	0.03	19.78	0.06	19.86	0.03	bhb
202047	15:16:07.53	67:47:21.5	19.96	0.06	19.43	0.09	19.86	0.06	bhb

<sup>a</sup>The complete version of this table is in the electronic edition of the Journal. The printed edition contains only a sample.

<sup>b</sup>J2000.0

TABLE 2  
NUMBER OF COLOR-COLOR SELECTED GIANTS IN RGB  
BOUNDING BOX

$\Delta M$	Number of Giants		
	$M_0 < 19.3$	$M_0 < 19.65$	$M_0 < 20.0$
-0.33	267	392	486
-0.66	121	223	311
-0.99	47	98	183
-1.32	33	50	83
-1.65	34	41	50
-1.98	24	34	36
-2.31	25	28	29
-2.64	23	31	22
-2.97	25	28	23

TABLE 3  
URSA MINOR GIANT CANDIDATE COUNTS AND BACKGROUND LEVELS

Magnitude Limit	UMi Giant Counts	Area deg <sup>2</sup>	Extratidal <sup>a</sup> Counts	Area <sup>b</sup> deg <sup>2</sup>	Background deg <sup>-2</sup>
$M_0 \leq 19.3$	393	9.06	100	8.06	$3.1 \pm 0.6$
$M_0 \leq 19.65$	540	8.31	139	7.31	$4.0 \pm 0.7$
$M_0 \leq 20.0$	600	5.56	119	4.56	$5.2 \pm 1.0$

<sup>a</sup>Stars found outside the IH95 tidal radius

<sup>b</sup>An ellipse drawn from either the IH95 or K98 structural parameters has area of  $\sim 1$  deg<sup>2</sup>.

TABLE 4  
 STAR COUNTS OF URSA MINOR GIANT CANDIDATES IN ELLIPTICAL ANNULI

$r_{in}$ arcmin	$r_{out}$ arcmin	$M_0 \leq 19.3$		$M_0 \leq 19.65$		$M_0 \leq 20.0$	
		Area arcmin <sup>2</sup>	Counts	Area arcmin <sup>2</sup>	Counts	Area arcmin <sup>2</sup>	Counts
0.0	3.4	16.2	9	16.2	14	16.2	19
3.4	6.8	48.6	28	48.6	37	48.6	42
6.8	10.2	81.0	39	81.0	51	81.0	62
10.2	13.6	113.4	28	113.4	48	113.4	62
13.6	20.4	323.9	68	323.9	100	323.9	115
20.4	27.2	453.5	43	453.5	54	453.5	70
27.2	34.0	583.1	32	583.1	47	583.1	54
34.0	40.8	712.7	17	712.7	19	712.7	19
40.8	47.6	842.3	19	842.3	21	842.3	27
47.6	54.4	971.8	15	971.8	17	971.8	19
54.4	61.2	1101.4	8	1101.4	12	993.6	16
61.2	68.0	1231.0	10	1217.3	13	996.9	14
68.0	74.8	1360.6	8	1265.6	11	989.3	10
74.8	81.6	1490.2	5	1219.1	6	994.9	4
81.6	88.4	1619.7	9	1249.5	10	1026.2	11
88.4	95.2	1730.0	5	1309.5	8	1059.5	9
95.2	122.4	7232.9	18	6583.8	20	4427.9	25
122.4	149.6	6837.0	20	6747.8	30	2788.3	19
149.6	176.8	6328.6	8	6118.5	14	2875.5	2
176.8	204.0	7704.5	1	7320.7	4	3860.9	1